

Active control of near-wall turbulence by local oscillating blowing

By SEDAT F. TARДУ

Laboratoire des Écoulements Géophysiques et Industriels (LEGI), BP 53 X 38041,
Grenoble-Cédex, France

(Received 12 March 1999 and in revised form 2 October 2000)

The effect of time-periodical blowing through a spanwise slot on the near-wall turbulence characteristics is investigated. The blowing velocity changes in a cyclic manner from 0 to 5 wall units. The frequency of the oscillations is nearly equal to the median frequency of the near-wall turbulence. The measurements of the wall shear stress and the streamwise velocity are reported and discussed. The flow field near the blowing slot is partly relaminarized during the acceleration phase of the injection velocity which extends 40 wall units downstream. The imposed unsteadiness is confined to the buffer layer, and the time-mean structural parameters under unsteady blowing are found to be close to those of isotropic turbulence in this region. The relaminarized phase is unstable and gives way to a coherent spanwise structure that increases the shear from 80 to 300 wall units downstream of the slot in a predictable way. This phenomenon is strongly imposed-frequency dependent.

1. Introduction

It has recently been shown through direct numerical simulations that it is possible to control near-wall turbulence by either using suboptimal schemes (Bewley *et al.* 1993; Hill 1993, 1994) or adaptive nonlinear methods (neural networks, Lee *et al.* 1997). These studies lead to some insight into the near-wall physics, but somewhat indirectly. There are, however, some ‘feasibility’ problems from a technological point of view. The physical application of these methods requires an unacceptably dense distribution of the sensors and actuators at the wall. The streamwise and spanwise spacing of these micro electro-mechanical systems (MEMS) have to be as small as the viscous sublayer thickness to obtain an appreciable drag reduction of about 20%. Therefore, and despite the progress achieved now in micro-technology, the feasibility of these control strategies is still under question.

One way to remedy this situation could be the use of a robust-control-like strategy by first slightly forcing the near-wall turbulence, then determining its frequency response and, finally, introducing local suboptimal control with eventually a coarser and feasible distribution of MEMS depending upon the reaction of the near-wall flow. This study deals with the first of these, namely the reaction of the near-wall turbulence to a time-periodical forcing through a localized oscillating blowing. The achievement of this strategy poses the problem of optimal control of periodically perturbed (cyclostationary) flows, which is an interesting theoretical challenge.

The active and passive management of the turbulent wall shear stress is ultimately related to the interaction of the coherent structures present in the inner layer with the near-wall flow. The *ad hoc* out-of-phase active control scheme reported by Choi, Moin

& Kim (1994) may, for instance, be replaced easily in this context. The wall shear stress is instantaneously enhanced in the regions where the spanwise vorticity is stretched through the stagnation flow induced by the quasi-streamwise (QSV) Reynolds shear stress producing vortices (see for example Tardu 1995 and the references therein). Drag reduction can be achieved by decreasing the intensity of the QSVs or by pushing them away to weaken their interaction with the near-wall flow. A time-periodical localized blowing through a slot provides in this sense a supplementary parameter that is the imposed frequency of the oscillations. Here, we discuss how the suboptimal schemes may be modified to incorporate the effect of a continuous time-dependent intervention at the wall.

Studying local excitation of the near-wall turbulence may help us to solve problems related to controllability and predictability. Rendering a process predictable (or deterministic-like) increases its degree of controllability. It is known that any unpredictable process $s[n]$ can be decomposed into $s[n] = s_x[n] + s_\beta[n]$, where $s_x[n]$ is a regular process and $s_\beta[n]$ is a predictable process orthogonal to $s_x[n]$. This result is known as Wold's decomposition (Papoulis 1984 p. 441). In the case of near-wall turbulence $s_\beta[n]$ may be interpreted as the part due to the coherent structures, while $s_x[n]$ is the incoherent part. The aim of a pseudorobust control is to intervene locally in space somewhere at the wall to filter $s_x[n]$, to accentuate $s_\beta[n]$, and to control the flow more efficiently at further downstream locations.

This strategy is in keeping with the general pattern of dual control, a technique used in some stochastic optimal control solutions (Bar-Shalom 1981; Stengel 1994 p. 436). The aim of dual control is to provide control inputs that enhance parameter estimation in real-time and adapt the control strategy accordingly. The *ad hoc* system inputs, such as impulses, doublets, time-periodical waveforms inject energy in the system to improve its predictability and identifiability. These inputs, exactly as the time-periodical, space-localized blowing investigated here, may allow better future state estimates and control actions. The dual control may provide 80% more accurate results in some applications, compared with control without probing commands (Tse & Shalom 1973).

The details of dual control are given in Bar-Shalom (1981) and Maitelli & Yoneyama (1999) and references therein. We only aim to clarify the possible role of local excitation of the near-wall turbulence as a probing strategy. We introduce in figure 1, adapted from Stengel (1994), the block diagram of dual control using the local unsteady blowing as probing input. A predicted state \hat{x} corresponds to each step of the process. The nominal control u_0 is the optimal deterministic trajectory (i.e. without taking into account the uncertainties) related to the predicted state. Because of the uncontrollable uncertainties (turbulence), the control should be cautious. The cautious cost depends upon the covariance of the state equations, as well as the subsequent process noise. The probing is obtained by experimentation and its aim is to reduce the future uncertainties, i.e. the updated covariance and the value of the future information. The dual control provides more accurate parameter estimates because of less cautious control activity. Thus, we can claim that the local unsteady blowing is an efficient probing if it decreases the covariance in some extended zone downstream of the intervention. It will be shown in this study that this is indeed the case in a significant region, but that there is a subsequent penalty. Possible solutions will be discussed.

We will now give a concrete example. Recently, some controllers have been developed using the linearized Navier–Stokes equation. This is because the linear coupling term plays an important role in the vorticity generation mechanism. Some 10% drag reduction has been obtained through the control of part of the modes (Lim *et al.*

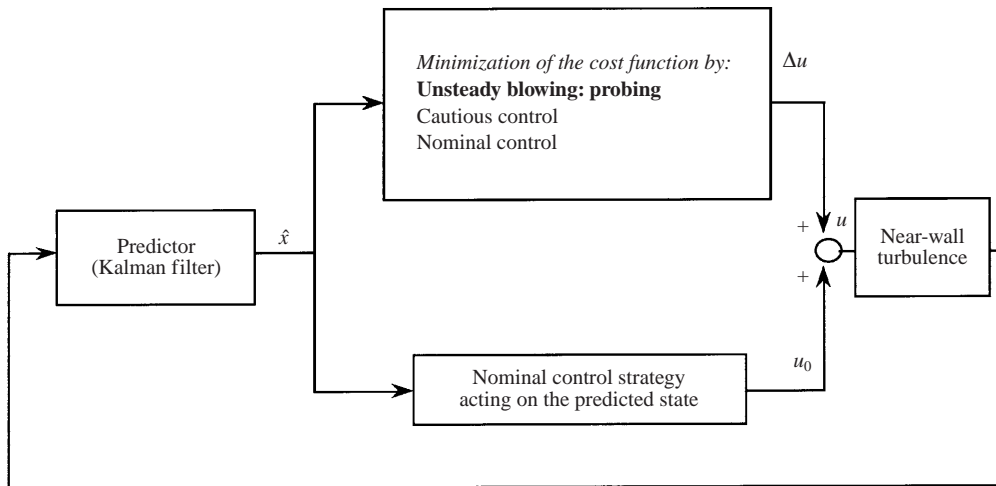


FIGURE 1. Principle of dual control with unsteady localized blowing used as probing control. The system anticipates a future decision by using a Kalman filter as predictor. The nominal control u_0 is the optimum deterministic strategy on the estimated state \hat{x} without turbulence. The cautious control is imposed by turbulence. The probing aims to reduce uncertainty.

2000). The dual control in this sense is envisaged as follows. The stochastic controller can, for instance, be a linear-optimal controller as used by Lim *et al.* (2000). This can be extended with a Kalman–Bucy filter that estimates parameters and state. The probing is provided by localized unsteady blowing–suction to enhance the state estimation and improve the cautious control actions. The latter may still be achieved by ‘pinpoint’ blowing–suction as used in suboptimal schemes. Since probing enhances the parameter estimation, it is expected that the cautious control requires fewer sensors and actuators.

New perspectives are possible in near-wall turbulence control. The objectives of this preliminary study are, however, limited to clarifying the following points:

- (i) the efficiency of localized unsteady blowing as an open-loop control scheme;
- (ii) the frequency response of near-wall turbulence subject to a localized blowing from slots and the related flow phenomena;
- (iii) the efficiency and limitation of unsteady blowing as a probing method to enhance the predictability.

Large-scale unsteady blowing is already used in separation control. However, the response and the relaxation of the near-wall turbulence to a localized intervention at the wall are not well understood even when the latter is steady (Sano & Hirayama 1985; Pailhas *et al.* 1991; Sokolov & Antonia 1993; Choi, Park & Hahn 1997). Space-periodic local suction and blowing to control the near-wall turbulence is not an original idea. One example is the selective suction in the spanwise direction proposed by Gad-el-Hak & Blackwelder (1989). The addition of time periodicity that renders the relaxation phenomena depending on both time and space is, however, new, at least in the context of the near-wall control.

2. Definitions, experimental set-up and data reduction

2.1. Experimental set-up

An experimental model has been developed in the wind tunnel of our laboratory (figure 2a). The blowing at the wall is done through a spanwise slot of $L_x = 0.6$ mm

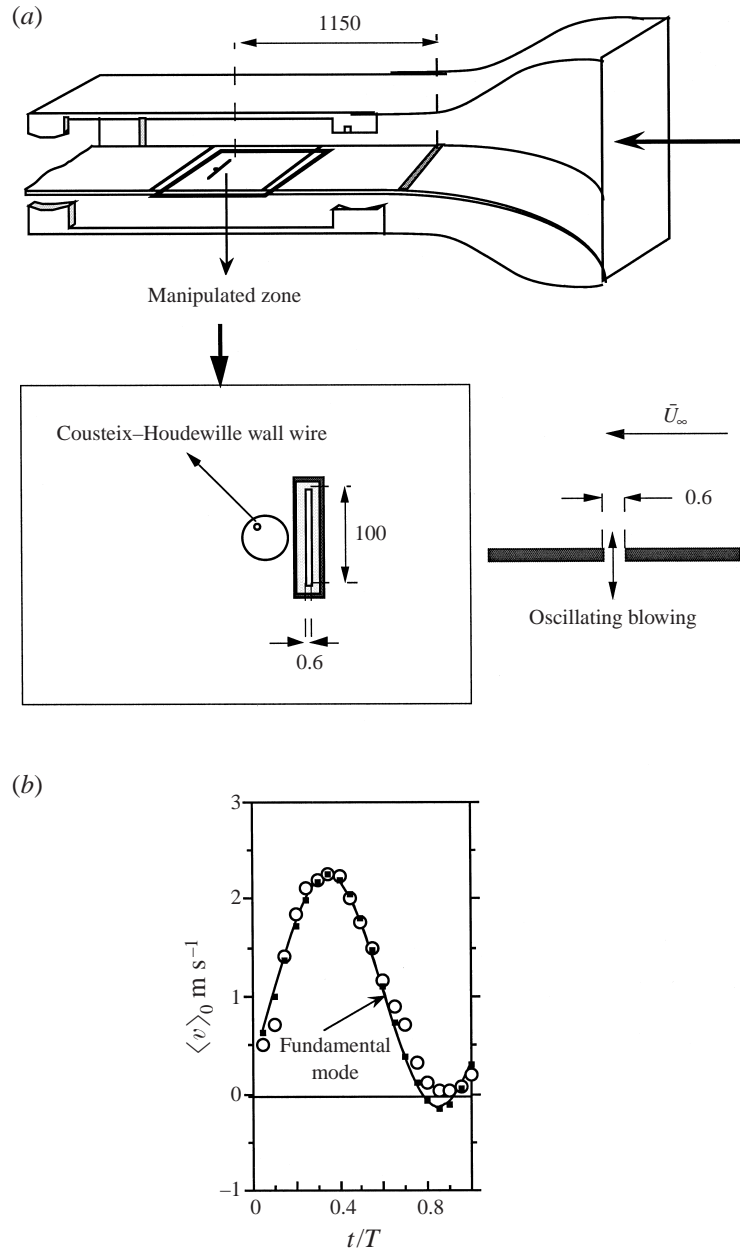


FIGURE 2. Experimental set-up. (a) Wind tunnel and test section. The dimensions of the blowing slot are shown in mm. (b) Example of phase average of the injection velocity. The imposed frequency in wall units is $f^+ = 0.017$.

streamwise width and $L_z = 100$ mm spanwise length. These dimensions correspond, respectively, to $L_x = 7l_v = 7(\nu/\bar{u}_\tau)$ and $L_z = 1212l_v$ when the external velocity is $\bar{U}_\infty = 4 \text{ m s}^{-1}$ (nominal working conditions), where ν is the kinematic viscosity and $\bar{u}_\tau = \sqrt{(\tau/\rho)}$ is the shear velocity. The test station is situated $13938l_v$ downstream of the tripping strip.

A special pulsating device has been designed for the present purpose. It consists of a profiled cylinder mounted on a shaft driven by a variable speed motor. The cylinder covers some, all, or none of the length of the slots to produce a periodical normal velocity of suction and blowing. Compressibility waves have been avoided by making use of ‘acoustical filters’ at the outlet of the pulsating device. The volume of these settling chambers may be changed according to the desired value of the cut-off frequency. Quite satisfactory sinusoidal waveforms of the suction/blowing wall normal velocities $\langle v_0 \rangle$ have been obtained in this way for the amplitude of the imposed wall normal velocities up to $\hat{A} = A_{\bar{v}_0} = 2 \text{ m s}^{-1}$ ($\hat{A}^+ = 8$) and the imposed frequency $f < 50 \text{ Hz}$ ($f^+ < 23 \times 10^{-3}$) (figure 2*b*). Hereinafter ‘+’ denotes values scaled with the inner variables, i.e. the shear velocity and the viscosity.

The wall shear stress measurements have been performed by means of a Cousteix–Houdeville wall hot-wire gauge (HWG) to avoid problems caused by conduction into the substrate (see for example Tardu, Pham & Binder 1991). A wire of $4 \mu\text{m}$ diameter is set into a microcavity and flush mounted to the wall (figure 25 of the Appendix). The length of the sensing element is $200 \mu\text{m}$ which corresponds to a spanwise extent of $\Delta_z^+ \approx 3$ at the test station with $\bar{U}_\infty = 4 \text{ m s}^{-1}$. It is well known that $\Delta_z^+ < 20$ to avoid problems caused by the spanwise averaging of the energetic structures. It is seen that the dimensions of the HWG sensing part are largely within this limit. It is shown in the Appendix that consistent results up to the statistics of order 4 are obtained with this probe. The streamwise velocity is determined by a TSI 1276-10W micro hot film. The sensing element of the later is 5 wall units.

The sampling frequency was set equal to $f_s^+ = 2$. A Krohn Hite filter at adequate cut-off frequencies prefiltered the signals. The total duration of each record is $T_{tot} \approx 5000 T_\infty$ in the case of steady blowing and in the standard boundary layer where $T_\infty = \delta/\bar{U}_\infty$ is the outer timescale. This is long enough to ensure the convergence of the statistics up to fourth-order moments including those of the time derivative of the fluctuating signals (Klewicki & Falco 1990). The total duration of the data was increased up to $T_{tot} \approx 25\,000 T_\infty$ in the case of unsteady blowing to guarantee the statistical convergence of the phase averages. Bucking amplifiers were used to suppress the d.c. anemometer output at zero velocity, so that the signal could be amplified before A/D conversion. This conversion was performed with an Analog-Device RTI-800 board (accuracy: 11 bit+sign; 8 channels) installed in a PC. The calibration of the HWGs was performed in situ.

Care is necessary in the interpretation of data in the presence of organized motion. To extract the deterministic and deduce the random part of the flow quantities, the classical triple decomposition is used. A flow quantity $q(\mathbf{x}, t; T)$ is decomposed into a time mean \bar{q} , an oscillating \tilde{q} and a fluctuating q' part:

$$q(\mathbf{x}, t; T) = \bar{q}(\mathbf{x}) + \tilde{q}(\mathbf{x}, t/T) + q'(\mathbf{x}, t),$$

where T is the period of the oscillating blowing. The ensemble or the phase average is performed to determine the amplitude $A_{\tilde{q}}$ and phase $\Phi_{\tilde{q}}$ of the oscillating part \tilde{q} :

$$\langle q(\mathbf{x}, t/T) \rangle = \bar{q}(\mathbf{x}) + \tilde{q}(\mathbf{x}, t/T) = \lim_{N \rightarrow \infty} \sum_{i=1}^N q(\mathbf{x}, t + iT),$$

from which the instantaneous fluctuating part q' is adequately determined. A pulse from a photoelectric cell triggered by the pulsator provided the beginning of each cycle, and the trigger signal was also recorded. The modulation characteristics have been determined through a least-squares Fourier analysis.

2.2. Experimental conditions; blowing severity

The results presented here are obtained with an imposed frequency $f^+ = fv/u_{\tau SBL}^2 = 0.017$, and an amplitude $\hat{A}^+ = 5$. The Reynolds number based on the boundary-layer thickness of the SBL is $Re_\delta = 10^4$, at the test section and the free-stream velocity is $\bar{U}_\infty = 4 \text{ m s}^{-1}$.

In flows with uniformly distributed continuous blowing/suction (transpired layers through a porous surface), the parameter that characterizes the intervention at the wall is given by $B_f = \bar{v}_0 \bar{U}_\infty / \bar{u}_\tau^2 = \bar{v}_0^+ \bar{U}_\infty^+$ where \bar{v}_0 is the injection/suction velocity at the wall (Andersen, Kays & Moffat 1975). This is expected, since B_f appears directly in the momentum integral equation of the transpired boundary layer and plays a role similar to the Clauser pressure-gradient parameter. However, the characterization of the severity of local blowing/suction by strips is not straightforward and B_f is not suitable for describing the flow characteristics past the local intervention, as clearly shown by Sano & Hirayama (1985) and Sokolov & Antonia (1993). Indeed, the local suction/blowing involves phenomena related to the relaxation of near wall turbulence downstream of the intervention zone. When \bar{v}_0^+ is low, but the injection is carried out over large areas as in transpired boundary layers, the flow has enough time to relax and reach its equilibrium state rapidly. On the other hand, in the case of large injection velocities \bar{v}_0^+ over short distances by strips, the near wall turbulence can hardly maintain its equilibrium state and its structure is expected to be strongly affected (Sokolov & Antonia 1993). Therefore, $B_f \propto \bar{v}_0^+ \propto \bar{v}_0 / \bar{U}_\infty$ cannot be a similarity parameter in such cases. The ratio of the injection or suction flow to the incoming flow rate, i.e.

$$\Theta = v_0 L_x / \int_0^\infty \bar{U} dy$$

is therefore introduced by the authors cited, and proved to be adequate for measuring the blowing/suction severity.

We proceeded with particularly small slot widths compared with previous studies quoted above. For instance, the experiments reported by Sano & Hirayama (1985) have been conducted with two different configurations wherein L_x was, respectively, 50 and 25 mm corresponding to $L_x^+ \approx 2000$ and $L_x^+ \approx 1000$ under their experimental conditions. Recall that the slit width is only $L_x^+ = 7$ here. Consequently, the severity parameter is low. The injection velocity in steady blowing experiments investigated here is $\bar{v}_0 = 1 \text{ m s}^{-1}$ and the severity parameter is only $\Theta = 0.006$. We measured the shape parameter just downstream of the slit at $x/\delta = 0.1$ under these circumstances and found $H = 1.4$. We concluded, therefore, that the flow is not separated, at least at this particular position. In unsteady blowing experiments, the injection velocity $\langle v_0 \rangle$ changes in a cyclic manner between 0 and 2 m s^{-1} . The maximum value of the severity parameter in the oscillation cycle is therefore $\Theta = 0.012$. The shape parameter measured at the same station increased to $H = 1.6$ at $\bar{v}_0 = 2 \text{ m s}^{-1}$, but still remained below the critical value corresponding to flows prone to separate. Note, by the way, that in DNS studies dealing with active control conducted so far, the severity parameter is zero, because of the pinpoint intervention. In practical situations this is impossible, and even a low Θ may affect profoundly the flow in the neighbourhood of the injection/suction region. This may be an additional reason to consider the DNS results with some caution.

2.3. Notation

Before discussing the results, the notation must be clarified. We have three flow configurations here, namely, the standard boundary layer (SBL), and the manipulated

x^+	Unsteady blowing		Steady blowing	
	$\bar{\tau}_P^*/\bar{\tau}_{SBL}$	$\sqrt{\tau'\tau_P^*/\bar{\tau}_{SBL}}$	$\bar{\tau}_S^*/\bar{\tau}_{SBL}$	$\sqrt{\tau'\tau_S^*/\bar{\tau}_{SBL}}$
20	0.55	0.15	0.64	0.14
40	0.67	0.17	0.67	0.16

TABLE 1. The time mean wall shear stress and wall shear stress intensity under time periodical (subscript P) and steady blowing (S) compared with the standard boundary layer (SBL).

boundary layer (MBL) under steady and unsteady local blowing. Quantities measured in the manipulated boundary layer will be denoted by an asterisk (*) which will be omitted if unnecessary. The subscripts S and P indicate, respectively, steady and time-periodical blowing, and $^+$ indicates quantities scaled with the wall variables, i.e. the viscosity and the shear velocity.

3. Results

One of the main aims of this study is to determine whether a periodic time-varying blowing of the form $\tilde{v}_0^+ = \hat{A}^+(1 - \cos 2\pi f^+ t^+)$ affects the near-wall turbulence characteristics when compared with a steady injection by slot with the same time-mean blowing velocity $\bar{v}_0^+ = \hat{v}_0^+ = \hat{A}^+$ resulting in the same time mean severity parameter $\Theta = \langle \Theta \rangle$. In other words, the question is whether the near-wall flow interacts at the mean with the imposed unsteadiness or not. Therefore, we will systematically compare the mean flow characteristics obtained with unsteady and steady blowing hereinafter.

3.1. Time-mean flow

Table 1 summarizes the results concerning the time-mean wall shear stress $\bar{\tau}$ and its turbulent intensity $\sqrt{\tau'\tau}$ under steady and unsteady blowing. The closest point to the blowing slot at which the wall shear stress could be measured is $x^+ = 20$. Thus, the results are given at two test sections, respectively, $x^+ = 20$ and $x^+ = 40$. It is seen that the time-mean characteristics are not altered by the imposed unsteadiness under the present experimental conditions. Both the time-mean wall shear stress and wall shear stress intensities are identical under steady and unsteady blowing, except at the nearest position to the slot where the unsteady blowing gives a slightly larger decrease in the drag. Note that the drag reduction is about 40% at the mean. The wall shear stress intensity is related to the wall shear stress of the standard boundary layer (SBL) in table 1. Since $\sqrt{\tau'\tau}_{SBL}/\bar{\tau}_{SBL} = 0.36$ in the SBL as shown in the Appendix, it may be concluded from table 1 that the decrease in the wall shear stress intensity is roughly 60% in the manipulated boundary layer at $x^+ < 40$.

Figure 3(a) shows the time-mean streamwise velocity profiles in the standard boundary layer and in the presence of steady or unsteady blowing at $x^+ = 40$ downstream of the slit. The velocity \bar{u} and the wall normal coordinate y are scaled with the local inner variables, i.e. by $\bar{u}_{\tau_{SBL}}$ in the SBL and $\bar{u}_{\tau_S^*}$ or $\bar{u}_{\tau_P^*}$ in the manipulated boundary layer. The first striking feature of the results summarized in figure 3(a) is the insensitivity of the time-mean streamwise velocity profiles to the imposed unsteadiness. It is indeed seen that both \bar{u}_S^{*+} and $\bar{u}_U^{*+} = \langle \bar{u} \rangle^+$ corresponding, respectively, to steady and unsteady blowing, collapse fairly well in the entire boundary layer.

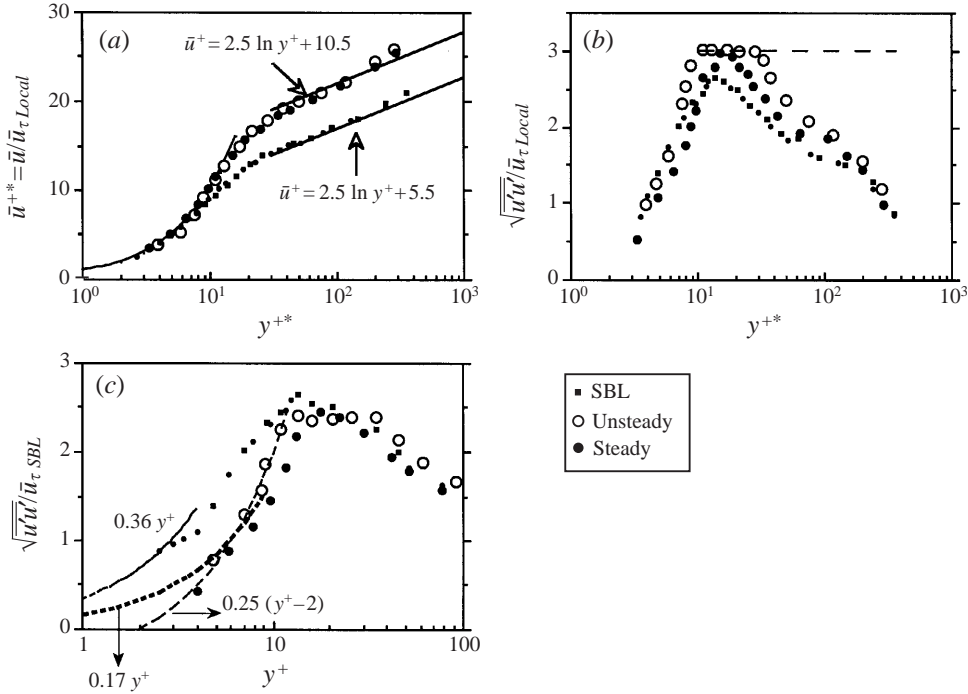


FIGURE 3. Time-mean velocity characteristics at 40 wall units downstream of the blowing slot. The imposed frequency is $f^+ = 0.017$ and the imposed amplitude is $\hat{A}^+ = 5$. (a) Time-mean velocity scaled with local shear velocity. (b) Longitudinal turbulent intensity versus the wall normal distance, both scaled with the local shear velocity. (c) Longitudinal turbulent intensity versus the wall normal distance, both scaled with the shear velocity of the standard boundary layer.

In figure 3(a), we can distinguish easily between the viscous sublayer, the buffer layer, and the log-layer in the manipulated boundary layer, in the same way as in the canonical boundary layer. These results lead us first to conclude that one of the major effects of the blowing is a considerable thickening of the viscous sublayer. Thus, $\bar{u}_S^{+*} \approx \bar{u}_P^{+*} = y^{+*}$ at $y^{+*} < 12$ under both steady and unsteady blowing while the thickness of the viscous sublayer in the SBL is 5 wall units. It is further noted from figure 3(a) that the velocity profiles collapse well with $\bar{u}^+ = 2.5 \ln y^+ + 10.5$ for $y^{+*} > 35$ in the MBL, pointing to the existence of a constant shear layer with time-mean equilibrium, leading to a logarithmic profile. The von Kármán constant is the same as the SBL. The buffer layer, on the other hand, is somewhat thinned and extends from only $y^{+*} = 12$ to $y^{+*} = 35$ under the effect of blowing. In the SBL, this layer occupies a larger zone restricted to $5 < y^+ < 30$.

The upward shift observed in the log region of the manipulated boundary layer agrees with the direct numerical simulations conducted by Choi *et al.* (1997) who investigated the effects of steady blowing and suction from a spanwise slot. This is a common feature of drag-reducing effects, and is a direct consequence of the thickening of the viscous sublayer and vice versa. This may be shown in different ways, for example by the Rotta model (1950). Rotta used the Prandtl mixing-length hypothesis and modelled the shear stress as $\partial \bar{u}^+ / \partial y^+ - \overline{u'v'}^+ = [1 + l_m^{+2} \partial \bar{u}^+ / \partial y^+] \partial \bar{u}^+ / \partial y^+ = 1$, where, contrary to the classical theory, the mixing length is, $l_m^+ = \chi(y^+ - \delta_v^+)$, where δ_v^+ is the thickness of the viscous sublayer in wall units, and χ is von Kármán's universal constant. The virtual origin of the mixing length is therefore shifted by δ_v^+ and the flow within $y^+ < \delta_v^+$ is supposed to be completely viscous. The streamwise

velocity distribution resulting from this closure is $\bar{u}^+ = A \ln y^+ + B$ at large values of y^+ with $A = 1/\chi$ and $B = (\ln 4\chi - 1)/\chi + \delta_v^+$. It is seen that B is directly related to the viscous sublayer thickness as expected. Taking $\chi = 0.4$ and $\bar{\delta}_{vS}^+ \approx \bar{\delta}_{vP}^+ = 12$ in the manipulated boundary layer, leads to $B = 10.6$, which is in close agreement with the results summarized in figure 3(a).

The distributions of the time-mean turbulence intensity $\sqrt{\overline{u'u'}}$ scaled with local variables are shown in figure 3(b). The profiles corresponding to the manipulated and standard boundary layers collapse in the aggregate, but there are some subtle differences in the reaction of the buffer sublayer turbulence to the unsteady blowing. It is first seen in figure 3(b) that the intensity under steady blowing is qualitatively similar to that of the unmanipulated boundary layer with a sharp maximum at $y^{+*} = 16$. In the SBL, $\sqrt{\overline{u'u'}}$ and the production reach their maximum at $y^+ = 12$, which is slightly smaller. The steady blowing increases the streamwise turbulence level in the low buffer layer apparently by about 10%. However, since the scaling is related to $\bar{u}_{\tau S}^*$, which decreases, the non-scaled maximum intensity is not or is only slightly affected, as can be seen in figure 3(c). The reaction of the buffer-layer turbulence to unsteady blowing presents one major characteristic, namely the intensity has a plateau in a large zone between $10 < y^{+*} < 50$. This indicates an unexplained increase of mixing near the wall caused exclusively by the imposed unsteadiness. The maximum, on the other hand, takes place at $y^{+*} = 10$, somewhat earlier than in the SBL.

Both the turbulence intensity and the wall normal distance y are scaled with the shear velocity of the SBL in figure 3(c) to show the raw effects of the manipulation. The behaviour near the wall is accentuated with the logarithmic scale. The data are consistent with those on the turbulent wall shear stress intensity. Indeed, the asymptotic behaviour of the turbulence intensity as the wall is approached is $\sqrt{\overline{u'u'}} \approx -\sqrt{\omega'_{z0}\omega'_{z0}}y$ with ω'_{z0} being the fluctuating spanwise vorticity at $y = 0$. This leads in wall units to $\sqrt{\overline{u'u'}}/\bar{u}_{\tau} \approx y^+ \sqrt{\overline{\tau'\tau'}}/\bar{\tau}$ as $y^+ \rightarrow 0$, with equality at $y^+ < 2.5$ (Popovich & Hummel 1967). Figure 3(c) shows that, in the SBL, $\sqrt{\overline{u'u'}}/\bar{u}_{\tau} \approx 0.36y^+$ very near the wall, as it should be. The first points next to $y = 0$, corresponding to the MBL, also collapse quite well with the linear curves whose slopes are equal to the values of $\sqrt{\overline{\tau'\tau'}}/\bar{\tau}_{SBL}$ taken from table 1. Only the curve (broken bold line) related to the unsteady blowing case is shown for the sake of clarity in figure 3(c).

The main effect of blowing is undoubtedly the shift of the flow structures away from the wall and, thereby, of the near-wall spanwise vorticity. The interesting feature of the streamwise turbulence intensity distribution under unsteady or steady blowing is its linearity in a large part of the near-wall layer demarcated by $4 < y^+ < 10$ (figure 3c). This gives the impression that there is a virtual origin situated at $y^+ = 2$, which may be related to the removal of the near-wall spanwise vorticity.

The effect of local oscillating blowing on the fine structure of turbulence is analysed through the distributions of the skewness and flatness factors of u' and of its time derivative, and the results are shown in figure 4. The time derivatives du'/dt are computed by using a 64-point digital finite impulse filter of zero phase shift. It has to be emphasized first that the measurements in the SBL are in excellent agreement with the literature (Ueda & Hinze 1975; Kim, Moin & Moser 1987). They are not shown in figure 4 for the sake of clarity. The global impression from the profiles obtained under steady blowing is that any effect on the fine structure is hardly detectable, except maybe close to the wall in the viscous region for the flatness of u' (figure 4b). Furthermore, there is clearly no dynamic structural effect of steady blowing on the small-scale turbulence, since the skewness of du'/dt collapses remarkably well with

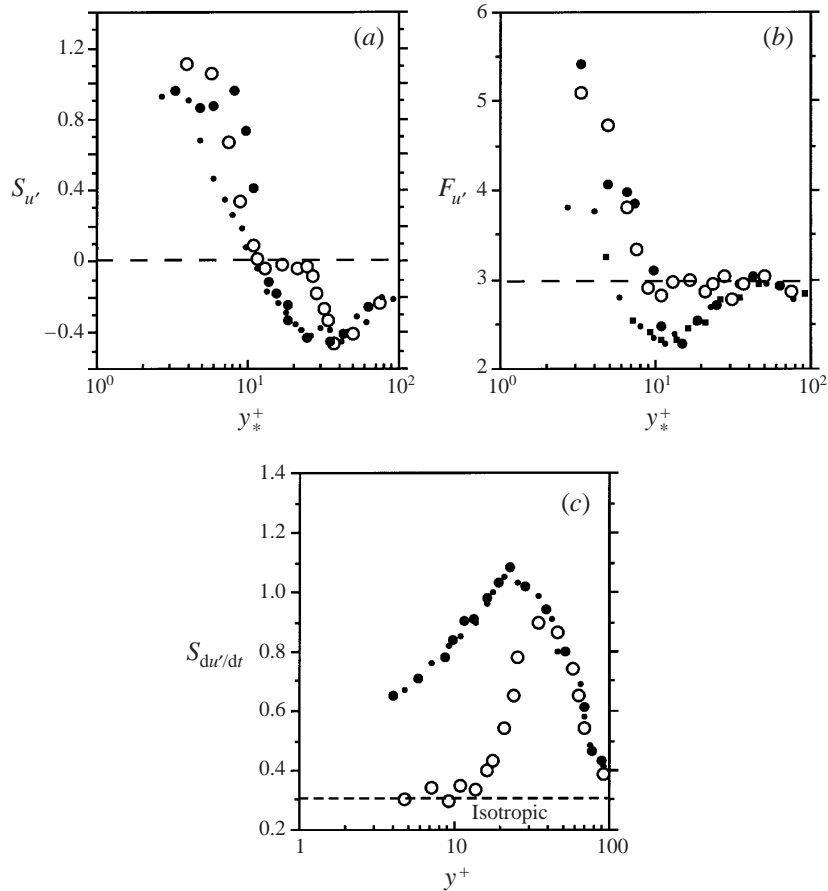


FIGURE 4. Fine structure of turbulence under unsteady and steady blowing. (a) Skewness, (b) flatness of fluctuating longitudinal. (c) Skewness of the time derivative of the streamwise fluctuating velocity. Symbols as in figure 3.

the SBL profile in figure 4(c). This is far from being the case for the oscillating blowing. The effect of the imposed unsteadiness in the whole buffer layer is indeed striking. The skewness and the flatness of u' at $10 < y^+ < 30$ are, respectively, $S_{u'} \approx 0$ and $F_{u'} \approx 3$ when the blowing is unsteady, compared with $S_{u'} \approx -0.3$ and $F_{u'} \approx 2$ of the SBL. Furthermore, the skewness of the time derivative du'/dt is found to be close to 0.3 in this zone, a value that is significantly different from 1 of the unmanipulated buffer layer (figure 4c). These results are remarkable because these characteristics are in fact those of isotropic turbulence. I am not aware of such a strong interaction caused by an excitation of any kind with the fine structure of the near-wall turbulence. The oscillating blowing acts presumably as an 'isotropening' (whitening) filtration at the time-mean sense near the wall under the present working conditions. The term 'at the mean' has to be emphasized since the flow quantities are strongly modulated in the buffer layer, as will be shown in the next section.

3.2. Phase averages

Figure 5(a) shows the cyclic modulation of the wall shear stress at $x^+ = 20$ and 40, downstream of the slit. The phase average $\langle \tau \rangle$ is scaled with the time-mean wall shear stress $\bar{\tau}_{SBL}$ of the unmanipulated standard boundary layer. The waveform of the

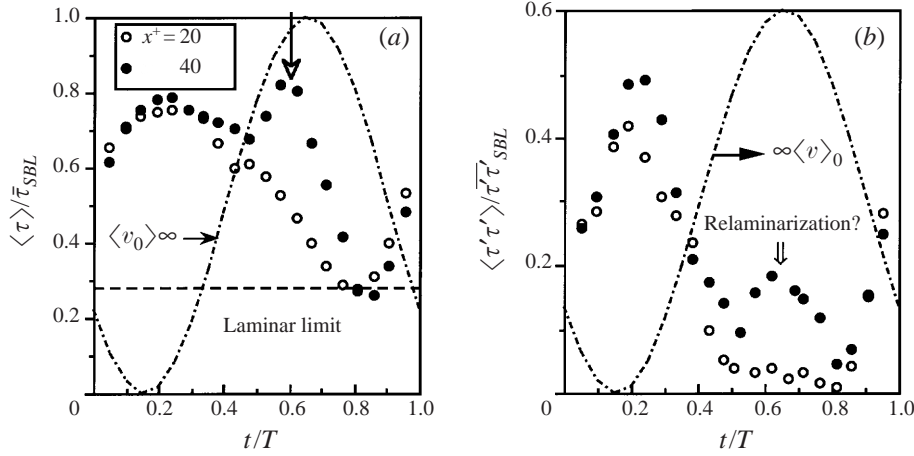


FIGURE 5. (a) Phase averages of the wall shear stress, and (b) wall shear stress intensity at $x^+ = 20$ and 40 downstream of the injection slit. The imposed frequency is $f^+ = 0.017$.

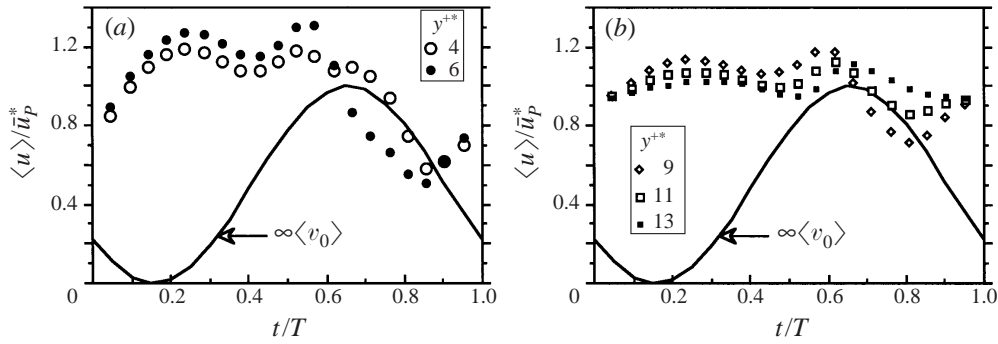


FIGURE 6. Modulation of the streamwise velocity at $x^+ = 40$, in (a) the viscous and (b) buffer sublayers.

injection velocity (not to scale) is also shown. The striking feature of the reaction of $\langle \tau \rangle$ takes place during the acceleration phase of the injection velocity. The wall shear stress decreases rapidly during this phase until it reaches the laminar limit defined as the value that a Blasius boundary layer would have at the same Reynolds number. The corresponding phase averages of the wall shear stress intensity $\langle \tau' \tau' \rangle / \bar{\tau}' \bar{\tau}'_{SBL}$ are shown in figure 5(b). The near-wall turbulence activity is totally suppressed at $x^+ = 20$ during half of the oscillation cycle, coinciding again with the acceleration phase of $\langle v_0 \rangle$. The decrease of the shear and of the suppression of the turbulence activity, point to a time-space localized relaminarization. At $x^+ = 40$, there is a slight increase both in $\langle \tau \rangle$ and $\langle \tau' \tau' \rangle$ at $t/T = 0.6$, shown by an arrow in figure 5. Close inspection of the data has shown that this corresponds to a transitional spot-like structure resulting from the set-up of an instability. This will be discussed in detail in § 3.3.

The phase averages of the streamwise velocity $\langle u \rangle (t/T; y^+)$ determined at $x^+ = 40$ are shown in figure 6. They are normalized by the local time mean velocity $\bar{u}_p^* (y^+)$ under unsteady blowing. They express, therefore, the relative modulation of $\langle u \rangle$. It is clearly seen in figure 6(a) that the phase average of the velocity decreases significantly during the acceleration phase, in agreement with the behaviour of the wall shear stress just discussed. The $\langle u \rangle$ modulation is large at $y^{+*} < 7$, and it is highly nonlinear

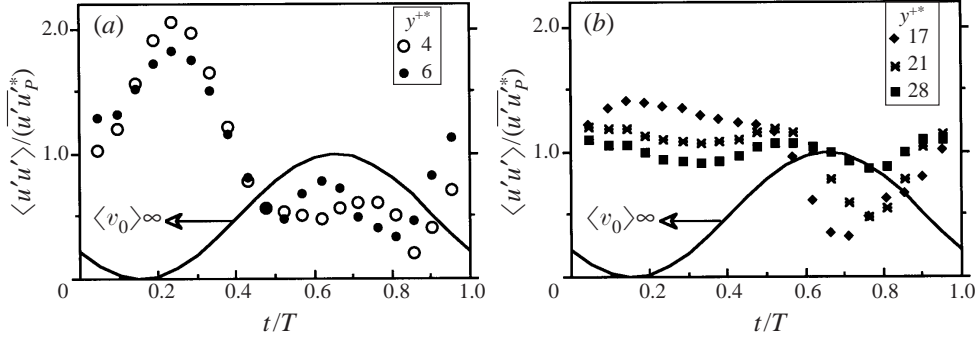


FIGURE 7. Modulation of the streamwise turbulence intensity at $x^+ = 40$. (a) Viscous sublayer. (b) Low-log layer.

with important secondary harmonics. It decreases rapidly in the low-buffer layer (figure 6b). At $y^{+*} = 13$, the relative amplitude of $\langle u \rangle$ is smaller than 10%. The penetration depth induced by oscillating blowing is about $\delta y^{+*} \approx 12$ at this particular x^+ station. The thickness of the zone wherein the oscillating shear is confined is of the same order of magnitude.

Figure 7 shows the phase averages of the streamwise turbulence intensity $\langle u'u' \rangle$ normalized by $\widetilde{u'u}_p^*$ to be consistent with the presentation adopted for $\langle u \rangle$. It is clearly seen in figure 7(a) that the viscous sublayer is almost free of turbulence activity during the acceleration phase. The other striking feature of the results presented in figure 7(a) is the occurrence of unexpectedly large modulations of the turbulence intensities that lead to peak-to-peak relative amplitudes as high as 80%. It is quite surprising to have such severe effects on turbulence when we recall that the unsteady $\langle v_0 \rangle$ forcing is only local. The $\langle u'u' \rangle$ modulation penetrates further in the low-log layer compared with $\langle u \rangle$ (figure 7b). The unsteadiness is not felt at $y^{+*} > 30$ where $\widetilde{u'u} \approx 0$.

The strong modification of the wall turbulence structure is captured better in figure 8 which shows the phase averages of the skewness $\langle S_{du'/dt} \rangle$ of the time derivative of fluctuating streamwise velocity du'/dt , and of the ejection frequency $\langle f_e^{+*} \rangle = \langle f_e \rangle v / \widetilde{u}_{\tau P}^{*2}$. The latter is identified by VITA through the phase-averaged thresholds at $y^+ = 12$ in a way similar to Tardu & Binder (1997). The detector function for VITA is:

$$D(t) = 1 \quad \text{if} \quad \sigma_v > k \langle u'u' \rangle \quad \text{and} \quad du'/dt > 0,$$

$$D(t) = 0 \quad \text{otherwise,}$$

where

$$\langle \cdot \rangle_v = 1 / \langle T_v \rangle \int_{t-T_v/2}^{t+T_v/2} \langle \cdot \rangle dt',$$

and $\sigma_v = (u^2)_v - (u'_v)^2$.

The threshold is set at $k = 0.35$ as in steady flow, according to Luchik & Tiederman (1987), while the integration time is equal to 13 wall units. The time of occurrence of a VITA ejection is taken as the middle of the $D(t)$ pulse. Only the accelerating events are taken into account. The thresholds were set respective to the phase average of $\langle u'u' \rangle$, and not to the time-mean turbulence intensity which would bias the results, as was shown by Tardu & Binder (1997).

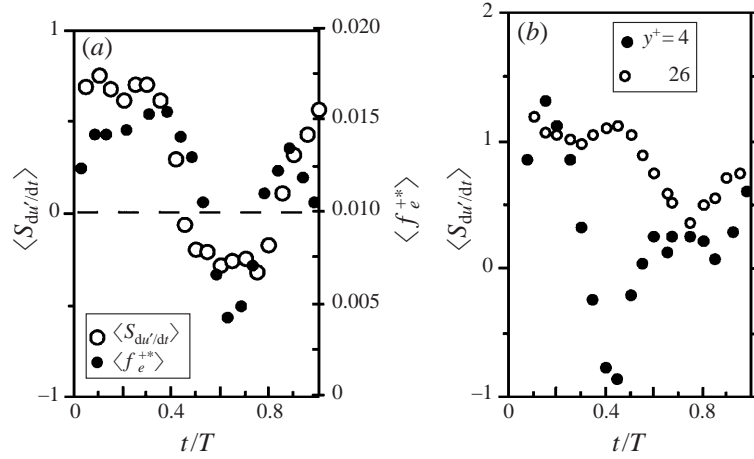


FIGURE 8. (a) Phase averages of the skewness of time derivative of u' and the ejection frequency determined by VITA using modulated thresholds as in Tardu & Binder (1997) at $y^+ = 12$ and $x^+ = 30$; the imposed frequency is $f^+ = 0.017$. (b) Phase averages of the skewness of the time derivative in the inner layer.

Coming to the results presented in figure 8, recall first that $\langle S_{du'/dt} \rangle$ is related to the production of mean-square streamwise vorticity by stretching and the nonlinearity in the inner layer (§4). Figure 8(a) shows that both the vorticity generation and production mechanisms are altered during half of the oscillation cycle. In the acceleration phase, the bursting activity, together with the vortex stretching, is largely suppressed. These effects are confined to the buffer layer, beyond which the modulation of flow quantities decreases sharply.

Further comments are required concerning the unusual behaviour of $\langle S_{du'/dt} \rangle$ shown in figure 8(b). It is clearly seen that $\langle S_{du'/dt} \rangle$ has large negative values at $0.4 < t/T < 0.8$ during the acceleration phase, contrary to the SBL wherein $S_{du'/dt} > 0$. Figure 8(b) shows that this effect is significantly pronounced in the buffer layer. In isotropic homogeneous turbulence, negative $S_{du'/dt}$ would mean inverse inertial transfer of energy across the wavenumber domain, and rapid destruction of the mean-square vorticity by compression, i.e. the suppression of nonlinear mechanisms. Such a strong reaction altering the fine structure of the turbulence has never been observed before to my knowledge. This point will be discussed further in §4.

Figure 9 shows the phase averages of the Taylor timescale defined as:

$$\langle \lambda_T^+ \rangle = \langle \lambda_T \rangle \bar{u}_\tau^2 SBL / \nu = \sqrt{\langle u'u' \rangle^+ / \langle (du'/dt)^2 \rangle^+},$$

together with the dissipation estimated through local isotropy by:

$$\langle \varepsilon \rangle_{iso}^+ = \langle \varepsilon \rangle_{iso} \nu^2 / \bar{u}_\tau^4 SBL = 15 \langle u'u' \rangle / \langle u \rangle^2 \langle \lambda_T^+ \rangle^2,$$

at $y^{+*} = 8$. The isotropic part of the phase-averaged dissipation is compared with the standard boundary-layer value, that is $\bar{\varepsilon}_{iso}^+ = 0.023$ at $y^+ = 8$. This agrees well with Antonia, Kim & Browne (1991). It is clearly seen that the isotropic dissipation increases by a factor 12 at the end of the acceleration phase of the injection velocity $\langle v_0 \rangle$, followed by a decrease of the Taylor timescale by a factor 2.

We should make a general remark here, relating both to some comments made before and to the measurement difficulties. The near-wall turbulence is highly anisotropic and the isotropic dissipation contributes only by some 20% to $\bar{\varepsilon}^+$ in the low buffer

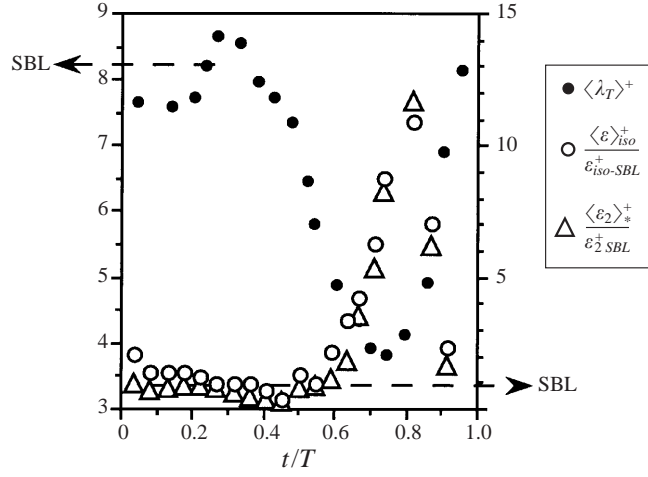


FIGURE 9. Phase averages of the Taylor timescale and dissipation estimated from local isotropy at $x^+ = 40$ and $y^+ = 8$; the imposed frequency is $f^+ = 0.017$.

layer (Antonia *et al.* 1991, figure 12). For the same reasons, $\langle S_{du'/dt} \rangle$, discussed previously, is only qualitatively related to the stretching mechanism, although it is a strong indicator of nonlinearity. We cannot give more exact details on these quantities with existing experimental means. The whole phenomenon studied here is mainly confined to the low buffer layer. In order, for example, to analyse the dissipation in detail, we need statistics related to $\partial u'/\partial y$ at $y^+ < 8$. This term is the easiest dissipation term to determine experimentally, but it can be measured reasonably well only outside the buffer region by a pair of parallel hot wires (Antonia *et al.* 1991). A distance of at least $\Delta y^+ = 4$ is required to avoid both the flow and thermal boundary-layer interferences, and that is why such a tentative result would be meaningless. To explain why more detailed flow quantities, including the flow visualizations or PIV data, could not be obtained here, we should emphasize that the thickness of the viscous sublayer ($y^+ = 5$) is 0.4 mm under the present experimental conditions. However, the lack of finer measurements does not discredit the previous physical arguments. There is a strong effect of imposed unsteadiness on the fine structure, of orders of magnitude.

It is possible to give a more accurate approximation of $\langle \varepsilon \rangle$. By analysing the terms of the dissipation tensor and using the DNS data at two Reynolds numbers, Antonia *et al.* (1991) have shown that the quantity,

$$\bar{\varepsilon}_2 = 2\nu \frac{\overline{\partial u'^2}}{\partial y} + \frac{11}{15} \bar{\varepsilon}_{iso},$$

is closer to the dissipation near the wall than the isotropic term alone. A crude approximation of the first term replaced by its wall value leads to:

$$\bar{\varepsilon}_2 = \frac{2}{\rho} \overline{\tau' \tau'} + \frac{11}{15} \bar{\varepsilon}_{iso}.$$

This approximation is acceptable only in the viscous and low buffer sublayers. The unsteady data have to be scaled with the phase-averaged inner variables for a rigorous comparison with the standard boundary layer. Therefore, we should compare $\langle \varepsilon_2 \rangle_*^+ = \mu^2 \langle \varepsilon_2 \rangle / \langle \tau \rangle^2$ with $\bar{\varepsilon}_{2-SBL}^+ = \mu^2 \bar{\varepsilon}_2 / \bar{\tau}_{SBL}^2$. The triangles in figure 9 show the ratio

$\langle \varepsilon_2 \rangle_*^+ / \bar{\varepsilon}_{2,SBL}^+$, which collapse surprisingly well with $\langle \varepsilon \rangle_{iso}^+ / \bar{\varepsilon}_{iso}^+$. The conclusion is still that there is increase of dissipation during the acceleration phase.

The comparison of figures 8 and 9 indicates that there is a complete lack of equilibrium at $0.4 < t/T < 0.8$ since the dissipation and the production (supposed to be proportional to the ejection frequency) are in opposition of phase. This is a common behaviour in high-frequency unsteady flows where large time lags exist between cause and effect mechanisms, as, for example, in channel flows subjected to an oscillating pressure gradient (Tardu & Binder 1997). The decrease of the Taylor timescale coincides with the decrease of the ejection frequency (i.e. the increase of the ejection period) showing that small-scale turbulence dominates the acceleration phase. Curiously, both $\langle \varepsilon \rangle$, $\langle \lambda_T \rangle$, $\langle f_e \rangle$ and $\langle S_{du'/dt} \rangle$ are constant at $t/T < 0.4$, i.e. until the middle of the acceleration phase, and these quantities remain more or less equal to those of the SBL when they are properly scaled with local inner variables. The strong modifications in the turbulence structure take place suddenly, once $\langle v_0 \rangle$ is accelerated sufficiently.

3.3. Birth of a coherent spanwise structure emerging from the relaminarized phase

The space–time evolution of the near-wall flow at locations further downstream is striking. First, the velocity profiles become strongly inflectional at $x^+ = 40$ and approximately in the middle of the deceleration phase. Figure 10(a) shows the phase-averaged velocity profiles at $t/T = 0.4$ (for reference) and at 0.8, corresponding, respectively, to the middle of the acceleration and deceleration phases of the injection velocity. The presence of an inflection point at $t/T = 0.8$ where $\langle \tau \rangle$ decreases to the laminar limit (figure 5a), is clear. It may, therefore, be argued that the relaminarized flow is possibly unstable to inviscid disturbances according to the Fjortoft theorem. This behaviour is somewhat consistent with the general idea that time or space deceleration destabilizes the flow (Shen 1961; Drazin & Reid 1981 p. 361). Figure 10(b) shows the y^{+*} distribution of the phase-averaged shear $\langle \partial u^+ / \partial y^+ \rangle = v / \bar{u}_{\tau,SBL}^2 \langle \partial u / \partial y \rangle$. Denoting the velocity at the point of inflection by $\langle u \rangle_I$, we have in the low-buffer layer $\partial^2 \langle u \rangle / \partial y^2 [\langle u \rangle - \langle u \rangle_I] < 0$ at $t/T = 0.8$, and this is a necessary (but not sufficient) condition of inviscid instability. It is emphasized here that close inspection of the phase-averaged streamwise velocity profiles shows that the local gradient is never zero, and that the vorticity does not change sign. Therefore, the observed behaviour is not due to a local unsteady separation according to the Moore–Sears criteria. Nowhere in the flow do the velocity and vorticity vanish simultaneously. Note in figure 10(b) that the extrapolation of the data to the wall indicates that the phase-averaged pressure gradient at $y = 0$ is $(1/\rho)(\partial \langle p_0 \rangle / \partial x) = v(\partial_0^2 \langle u \rangle / \partial y^2) = 0$. Therefore, there is no trace of an adverse pressure gradient induced by oscillating blowing that may lead to separation at $x^+ = 40$.

The destabilized flow enters subsequently a retransition region further downstream following the scheme reported by Narasimha & Sreenivasan (1973). This leads to the accumulation and enhancement of a patch of spanwise vorticity of the opposite sign to the mean vorticity during the deceleration phase at $t/T = 0.8$. The existence of this coherent patch may be seen clearly by the local maximum and minimum appearing in the $\sqrt{\langle u'u' \rangle} / \bar{u}_{\tau,SBL}$ profile shown in figure 10(c). The fact that it is positive may be understood through the sudden changes in the skewness of u' shown in figure 10(d) and the mechanism suggested schematically in figure 11. This patch rolls up into a coherent structure $\Omega'_{z,COH} > 0$ at approximately $y^+ = 12$. Figure 11 gives a possible explanation of the effect of this coherent structure on the velocity profiles, where it is suggested that $\Omega'_{z,COH} > 0$ may accentuate the inflection. Similar

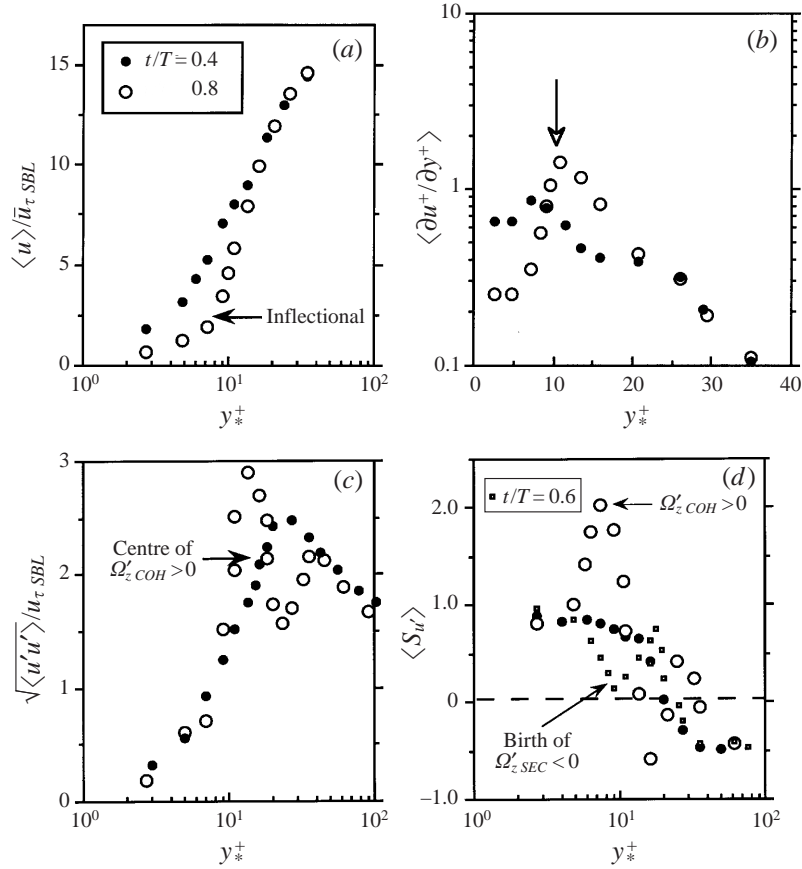


FIGURE 10. Distribution versus y^{+} of (a) the streamwise velocity, (b) the shear, (c) the streamwise turbulent intensity, and (d) the skewness of u' at $t/T = 0.4$ – 0.8 and $x^+ = 40$. The birth of $\Omega'_{z SEC} < 0$ is seen in (d) at $t/T = 0.6$.

scenarios wherein the roll-up of a structure occurs near an inflection point have been reported in studies involving vorticity-generation mechanisms (Ersoy & Walker 1985). The origin of $\Omega'_{z COH} > 0$ is situated at approximately $x^+ = 20$. Its birth, in turn, gives place downstream to a secondary spanwise vorticity layer near the wall with opposite sign, i.e. $\omega'_{z SEC} < 0$ because of the non-slip condition (see for example Doligalski & Walker 1978). We will show in the next section that this layer rolls up into a secondary coherent vortical structure $\Omega'_{z SEC} < 0$ in the far flow field and will accelerate the relaxation process. The genesis of the $\omega'_{z SEC} < 0$ layer and its subsequent development are well localized both in time and space. The vortex-ring-like structure, similar to the streamwise Falco typical eddy shown in figure 11, is likely in the far flow field where $\omega'_{z SEC} < 0$ is rolled up, but it is only suggested for the moment.

The whole structure is convected downstream, while $\omega'_{z SEC} < 0$ is reinforced and $\Omega'_{z COH} > 0$ diffuses somewhat more rapidly. The secondary wall vorticity layer induced by $\Omega'_{z COH} > 0$ through viscous effects is of the same sign as the pre-existing spanwise vorticity near the wall that is enhanced. Consequently, the wall shear stress increases almost in a Dirac function fashion at times and locations which are perfectly predictable as shown in figure 12(a). The near-wall turbulence activity increases also

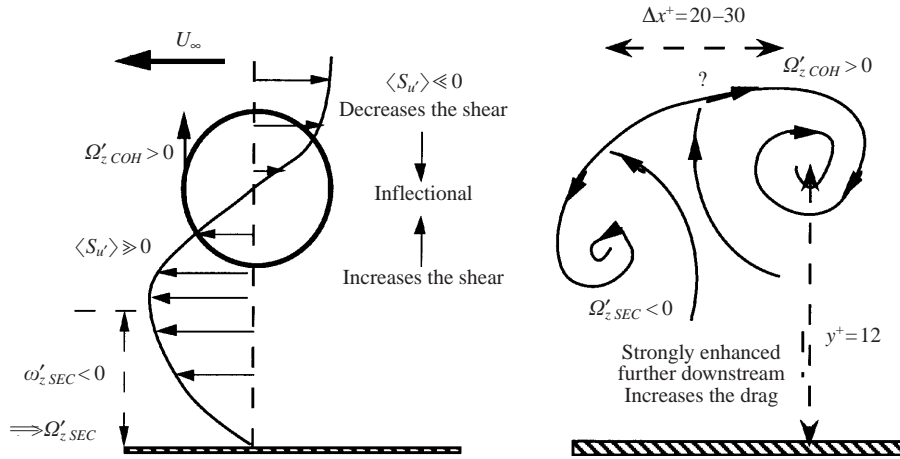


FIGURE 11. Possible mechanism of the genesis of the flow structure presumably associated with a shear layer instability during the relaminarization phase.

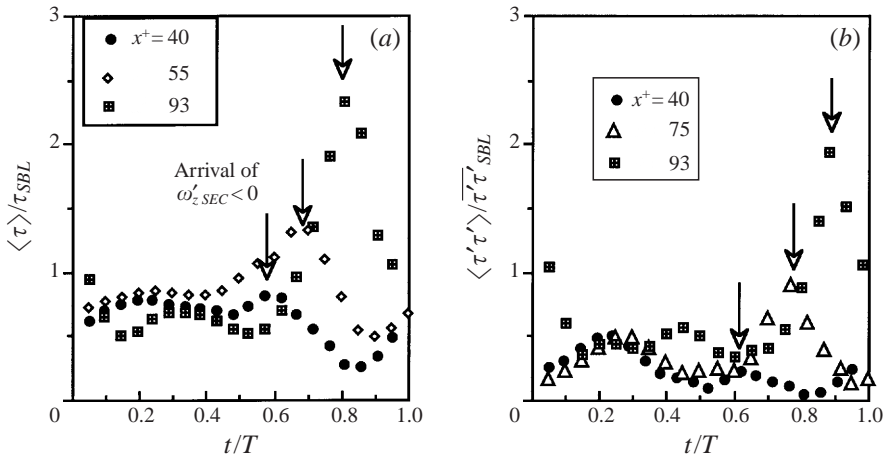


FIGURE 12. Phase average of (a) the wall shear stress and (b) the wall shear stress intensity at further downstream positions.

at the same times (figure 12b). Note, however, that $\langle \tau' \tau' \rangle / \overline{\tau' \tau'}_{SBL}$ is hardly larger than 1 at $x^+ = 75$, while the shear is already beyond the standard boundary-layer value at $x^+ = 55$, at which station the maximum $\langle \tau' \tau' \rangle$ is only $\langle \tau' \tau' \rangle / \overline{\tau' \tau'}_{SBL} = 0.5$ (not shown, to facilitate the reading). The unsteady localized blowing has a more favourable effect on the near-wall turbulence activity than the drag, at least in the near flow field.

The origin of the $\Omega'_{z,COH} > 0$ vortex is the positive primary vorticity layer $\omega'_{z,COH} > 0$ created immediately downstream of the slot. This layer is the direct consequence of localized blowing, whether it is steady or unsteady. It dilutes the existing negative spanwise vorticity near the wall, and that is why blowing decreases the shear. Under certain circumstances that will be discussed later, this vorticity layer concentrates, becomes confined in the low-buffer sublayer, and locally relaminarizes the flow. Further downstream, the vorticity assumes a distribution closer to its normal form. This implies that there is a vorticity discontinuity downstream of the relaminarized phase. The discontinuity being one of the necessary conditions for roll-up, it is

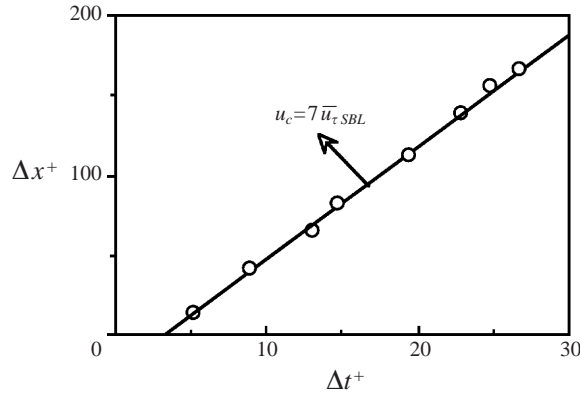


FIGURE 13. Travelling distance of the structure shown in figure 10 versus the time.

expected that the latter is set-up downstream. That may explain why the transition marked by the first stages of the roll-up and shown by the arrows in figure 5 comes before (i.e. downstream of) the relaminarization. A second plausible explanation is the following. Narasimha & Sreenivasan (1979 p. 285) have attributed the drop in the mean-square turbulent intensities and relaminarization by continuous blowing to the suppression of the intermittent Taylor–Görtler instability. The intermittent Taylor–Görtler instability is triggered by the sweeps that create, locally and intermittently, concave fluid trajectories. The blowing, in return, renders them strongly convex immediately downstream. Thus, the near-wall flow is stabilized very near the slot, but further downstream the intermittent stability mechanism remains less affected. Thus, it is potentially more capable of triggering the roll-up of the $\omega'_{zCOH} > 0$ layer.

Figure 13 shows the travelling distance versus the time determined from the intervals separating the peaks of the shear stress, marked by the arrows in figure 5. Note that there is almost no scatter in this figure. A structure advection velocity U_c of $7\bar{u}_{\tau SBL}$ can be deduced from these results, indicating that the structure merely is close to the wall. The whole phenomenon relaxes further downstream at $x^+ = 600$, as will be discussed in §3.5. This mechanism that acts as a vorticity pump occurs in the high-frequency regime, as we will show in §3.6. Therefore, it can nicely be used to increase the drag and prevent unsteady separation and/or to decrease it through distributed blowing locations and by frequency modulation with only negligible cost. On the other hand, the combination of phase-shifted blowing/suction at $x^+ > 40$ may be efficient for the space–time control of ω'_{zSEC} . A consistent scheme explaining the set-up of these phenomena is discussed in §4.3.

3.4. Development of the secondary vorticity layer and roll-up

The first roll-up stages of the secondary vortical structure are perceptible at $t/T = 0.6$ and $x^+ = 40$ in the phase-averaged skewness profiles shown by small squares in figure 10(d). An estimation based on the convection velocity and the time of appearance of the structures implies that the secondary structure occurs at 20–30 wall units downstream of $\Omega'_{zCOH} > 0$. Zhou *et al.* (1999) who investigated the generation of coherent hairpin packets through direct numerical simulations and stochastic estimation have recently reported a similar downstream generation mechanism. The roll-up is only partial at this stage, and the secondary structure is weak. The near-wall flow is still under the effect of the $\omega'_{zSEC} < 0$ layer created downstream of the primary structure. This secondary vorticity layer is confined to the low-buffer

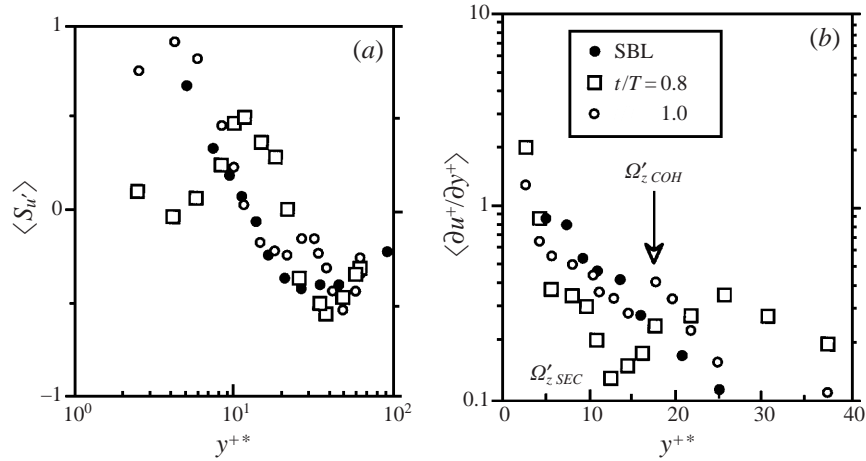


FIGURE 14. Roll-up of the secondary vorticity layer at $x^+ = 120$ and $t/T = 0.8$. The process is detected by (a) the large negative contribution to the skewness near the wall, and (b) a minimum that appears in the phase averaged shear. The primary structure at $t/T = 1$ is rather weak at this station.

layer and diffuses weakly. It enhances the wall vorticity that is of the same sign, and the shear increases drastically until $x^+ = 150$ (see § 3.5). Figure 14(a) shows the profiles of the phase-averaged skewness at $x^+ = 120$, the first test station that is just upstream. It is seen that there is a large discontinuity in $\langle S_{u'} \rangle$ at $t/T = 0.8$ with a large negative contribution for $y^{+*} < 7$ and a large positive contribution beyond. The phase-averaged skewness $\langle S_{u'} \rangle$ decreases to zero at $y^{+*} \approx 0$, while the skewness should be close to its maximum value, which is 1 in a standard near-wall flow. A local minimum appears in the phase-averaged shear at the same time and location (figure 14b). The situation is indeed just the opposite of that for the appearance of the primary structure discussed in § 3.3. A straightforward interpretation is that the secondary vorticity is now entirely rolled up into $\Omega'_{z,SEC} < 0$. Note that the first weak signs of $\Omega'_{z,SEC}$ were found at $y^{+*} = 20$ in figure 10(d), near the slot, while the structure is now at $y^{+*} = 12$, closer to the wall. The time of appearance $t/T = 0.8$ agrees perfectly well with the estimation $\Delta t/T = (\Delta x^+ / U_C^+) f^+$ based on the advection velocity $U_C^+ = 7$ found in the previous section. With $\Delta x^+ = 128 - 40 = 88$, the estimation gives $\Delta t/T = 2$, resulting in $t/T = 0.8$ at $x^+ = 128$, given that the structure first appeared at $t/T = 0.6$ and $x^+ = 40$ (figure 10d).

The primary structure $\Omega'_{z,COH}$ is pushed away from the wall and almost disappears at $x^+ = 128$, as shown by the circles in figure 14. We defined the positions of primary and secondary structures, respectively, by the local maximum and minimum of the shear. The oscillating local shears $\partial \bar{u}^+ / \partial y^+ = \partial \langle u \rangle^+ / \partial y^+ - \partial \bar{u}^+ / \partial y^+$ represent the strength of the vortices. The results are shown in figure 15 which illustrates well the weakening of the primary vortex by turbulent diffusion and the strengthening of the secondary one by the inducing vorticity near the wall. At the same time, the secondary structure moves closer to the wall (figure 15b) and the roll-over occurs when $\omega'_{z,SEC}$ is enhanced sufficiently. It has to be emphasized that the generation mechanism observed here differs from the viscous–inviscid interaction and the unsteady separation process caused by a vortical structure moving above the wall, as intensively investigated by the Lehigh group (Doligalski & Walker 1978). Although an inflection point is observed at the same time and location of $\Omega'_{z,COH}$, there is no zero shear location in the flow when neither the primary nor the secondary structure occurs. Therefore, there is no

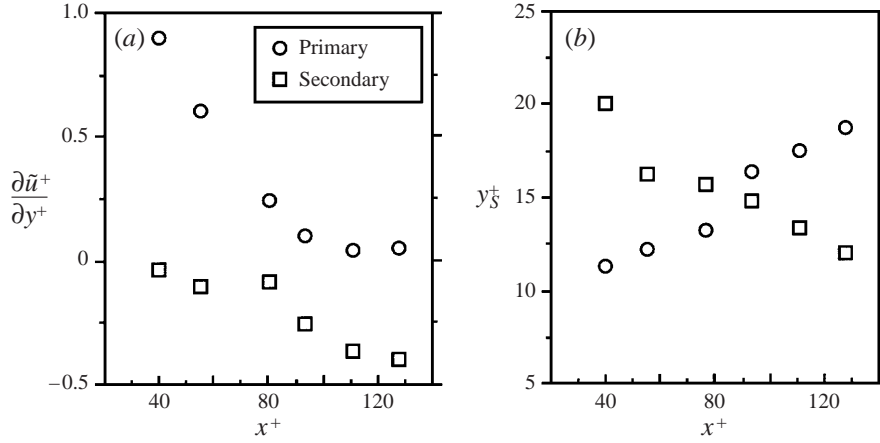


FIGURE 15. (a) The oscillating shear that corresponds to the \circ , primary and \square , secondary structures versus the streamwise distance from the slot, and (b) the wall normal position of the maximum and minimum of the shear describing the positions of the structures.

sign of an unsteady separation process. The vorticity is concentrated and there is a discontinuity in the corresponding layers strong enough to lead to roll-over. In that sense, the mechanism discussed here agrees well with Jiménez & Orlandi (1993).

The spanwise extent of the blowing slot is 10 times the streak spacing as indicated in §2.1. The flow is, therefore, *a priori* homogeneous in the spanwise direction. Indeed, we show in Appendix B, that the phase averages of the wall shear stress and of its turbulent intensity collapse over 86% of the slot spanwise extent $L_z^+ = 1212$ in the near flow field, and 92% in the far flow field. The $\langle u \rangle$ and $\langle u'u' \rangle$ measurements lead to the same results. That does not mean, however, that the triggering of the coherent spanwise structures discussed here is not affected by the singularities at the spanwise edges of the slot. We can imagine, for instance, that near the slot, these discontinuities lead to a horseshoe vortex whose head is precisely the spanwise structure that we detected. We are unable to reject or confirm this possibility. One comment that might lead to the rejection of this hypothesis is the following. In the case of a horseshoe (or a hairpin) vortex, the self-induced velocity field would normally push the head of the structure further away from the wall, at least into the low-log layer. However, we have always noticed that the coherent structures are within the low-buffer layer (figure 15b).

3.5. Relaxation mechanism

The effect of the secondary structure on drag should be opposite to that of the primary one, once it rolls up. In other words, Ω'_{zSEC} should decrease the drag and help the near-wall flow to recover somewhat more rapidly. To check this point, we summarized the flow characteristics in the far flow field in figure 16, by plotting the maximum peak phase-averaged values of the wall shear stress, and its turbulent intensity versus the streamwise distance. These quantities are related to the local values of the standard boundary layer. Once the ratios shown in figure 16 are equal to 1, there is no more modulation of the flow quantities and the relaxation is completed. We checked this point by further measurements in the buffer layer. The maxima are reached at $x^+ = 150$ as pointed out in the previous section. The secondary structure plays its drag-reducing role immediately downstream by exponentially decreasing $\langle \tau \rangle_{max}$. The

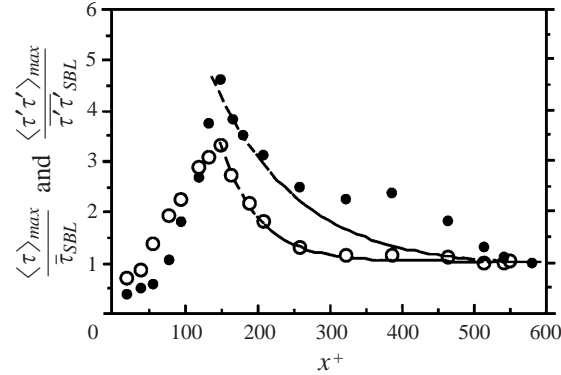


FIGURE 16. The ratios of the peaks of the wall shear stress and wall shear stress intensity versus the streamwise distance from the slot in wall units. ○, shear stress; ●, shear stress intensity; ---, regression exponential.

data collapse well with the dotted lines in figure 16 resulting from a least-squares exponential distribution. The agreement is particularly satisfactory at $x^+ < 350$. The increase of shear, on the other hand, is quite linear under the effect of the primary structure when $x^+ < 150$.

The turbulent wall shear stress intensity reaches values significantly larger than $\langle \tau \rangle_{max}$ at $x^+ = 150$. Its relaxation is slower. The maximum of the phase-averaged wall shear stress reaches the local standard boundary layer value at $x^+ = 400$. In return, it takes 200 wall units more for the near-wall turbulence to relax entirely. The exponential effect of Ω'_{zSEC} on $\langle \tau' \tau' \rangle_{max}$ ceases at $x^+ = 250$ at which position there is still significant modulation of the wall shear stress intensity.

3.6. Effect of the imposed frequency

The mechanism discussed in the previous section occurs when the blowing frequency is large. Figures 17(a) and 17(b) show the phase averages of the wall shear stress as a function of the imposed frequency near the actuator at $x^+ = 20$ and in the far flow field at $x^+ = 120$, respectively. The peaks in $\langle \tau \rangle$ at $x^+ = 120$ are observed only for the two largest frequencies $f^+ = 11 \times 10^{-3}$ and $f^+ = 17 \times 10^{-3}$. The wall shear stress intensity increases drastically at the same time, reaching values as large as $\langle \tau' \tau' \rangle / \bar{\tau}' \tau'_{SBL} = 3$, as discussed in §3.3. Therefore, there are good reasons to suppose a frequency threshold for the set-up of the primary structure Ω'_{zCOH} . To check this hypothesis, we conducted measurements by modifying the imposed frequency while keeping the other flow parameters the same. We counted a roll-up when we noticed the signature of induced ω'_{zSEC} through a sharp localized increase of $\langle \tau \rangle$. The measurements were performed at four locations in the range $80 < x^+ < 140$. The results are summarized in figure 18 by 0 when there is no roll-up, and by 1 otherwise. It is seen that a critical frequency $f_{cr}^+ = 8 \times 10^{-3}$ delimits the roll-up process. The critical frequency scaled with the local mean shear velocity is $f_{cr}^{+*} = f(v/u_{\tau Local}^2) = 14 \times 10^{-3}$. The transition from one regime to the other is discontinuous, if anything. Slight modifications near f_{cr}^+ trigger or suppress the roll-up.

The phase averages related to $f^+ > f_{cr}^+$ are remarkably similar in figure 17, suggesting that the reaction of the near wall flow remains the same beyond the critical frequency. In the low-frequency regime $f^+ < 5 \times 10^{-3}$, the reaction is globally similar too, especially in the near flow field and with a nonlinear response in the far

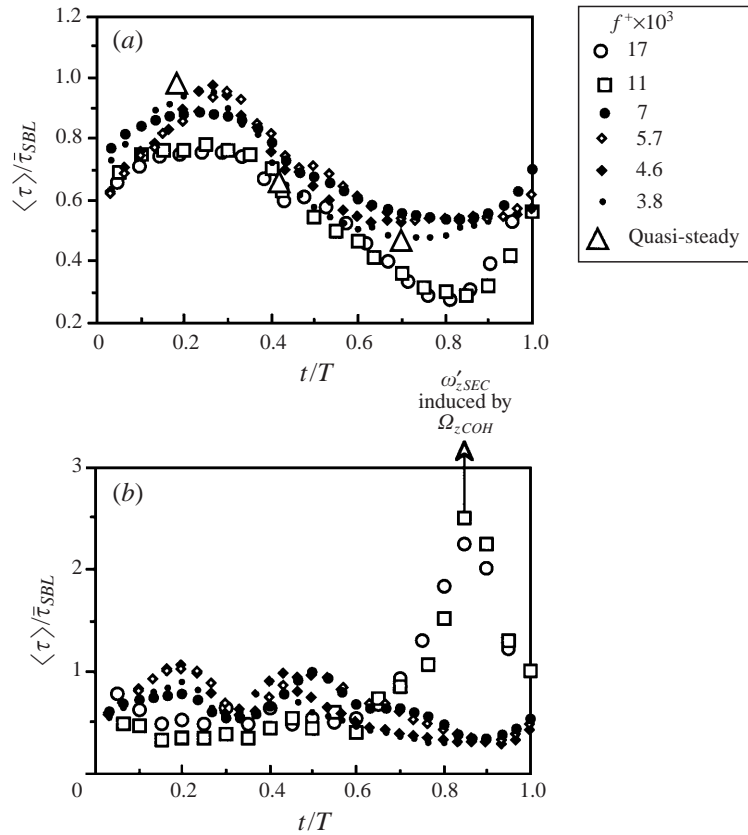


FIGURE 17. Phase averages of the wall shear stress at various imposed frequencies: (a) $x^+ = 20$, (b) $x^+ = 120$.

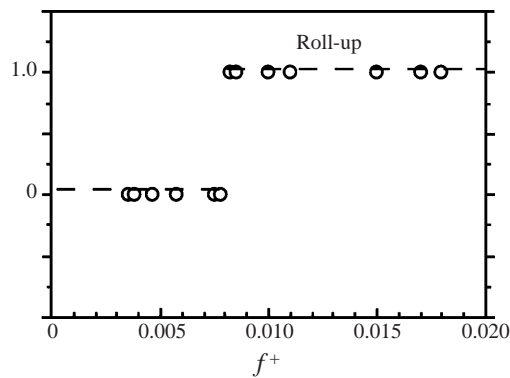


FIGURE 18. The critical frequency for roll-up is $f_{cr}^+ = 8 \times 10^{-3}$.

flow field revealed by high harmonics in $\langle \tau \rangle$ at $x^+ = 120$ (figure 17b). The flow at the smallest imposed frequency $f^+ = 3.8 \times 10^{-3}$ is in the quasi-steady regime. That is, the imposed unsteadiness is slow enough to allow the wall layer to adjust itself to the instantaneous blowing velocity. The three large triangles in figure 17(a) show the measurements when the blowing is steady at the corresponding phase averaged $\langle v_0 \rangle$,

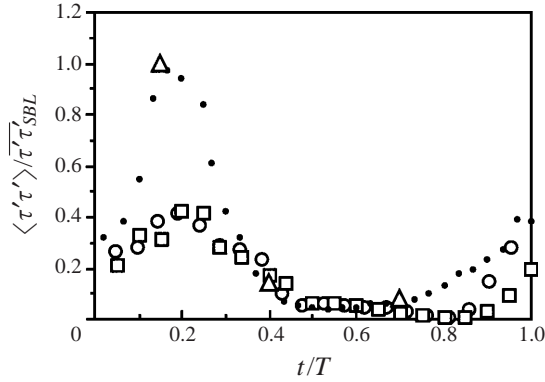


FIGURE 19. Phase averages of the wall shear stress intensity at $x^+ = 20$, and for different imposed frequencies. For symbols see figure 17.

namely, at $\langle v_0 \rangle^+ = 0$ ($t/T = 0.15$), $\langle v_0 \rangle^+ = 2.5$ ($t/T = 0.4$) and $\langle v_0 \rangle^+ = 5$ ($t/T = 0.7$). These measurements collapse with the unsteady ones at $f^+ = 3.8 \times 10^{-3}$, as it should be in the quasi-steady regime. The drag reduction does not vary exactly linearly with the severity parameter near the actuator with steady blowing. While the wall shear stress decreases by 36% at $v_0^+ = 2.5$ the decrease is only 58% when $v_0^+ = 5$.

The relaminarization effect of high-frequency blowing near the slot is clearly perceptible in figure 17(a). The confined primary vorticity layer ω'_{zCOH} decreases the shear by 30% at $t/T = 0.8$ with respect to low-frequency blowing. The effect on the wall shear stress intensity has to be more clarified. We show on figure 19 the cyclic modulation of $\langle \tau' \tau' \rangle$ at $x^+ = 20$. We have plotted the results corresponding to the largest and smallest imposed frequencies, to facilitate the reading. The phase averages for $f^+ < f_{cr}^+$ are reasonably similar. Note in figure 19 that the high-frequency unsteady blowing decreases the turbulent wall activity more than 50% at $t/T = 0.2$, which marks the beginning of the acceleration phase. There is also less turbulence activity at $0.6 < t/T < 1$, owing to ω'_{zCOH} (before the roll-up) and the finite-time relaxation of the near-wall turbulence.

There is an interesting issue regarding the far-flow-field development in the high-frequency regime. The wall shear stress phase averages at $x^+ = 120$ are systematically smaller when $f^+ > f_{cr}^+$ and prior to the arrival of the primary structure, i.e. at $t/T < 0.6$ (figure 17b). To quantify this feature, we computed the mean shear stress at $t/T < 0.6$ and defined the quantity

$$\bar{\tau}_{t/T < 0.6} = \frac{1}{0.6T} \int_0^{0.6T} \langle \tau \rangle dt,$$

which filters, in some way, the retrograde vorticity effect of the imposed unsteadiness on the drag. The open symbols in figure 20(a) show the corresponding results versus the frequency. They are grouped above and below the critical frequency, strengthening the previous remarks on the global similarity of the flow field in these regimes. It is clearly seen that there would be a gain of 20% in drag reduction by high-frequency blowing, if one could delay the Ω'_{zCOH} effect. In the high-frequency regime, the drag is significantly reduced during the acceleration phase near the slot. The relaminarized phase recovers more slowly and that explains the decrease of $\bar{\tau}_{t/T < 0.6}$ downstream for $f^+ > f_{cr}^+$. The conventional time-mean wall shear stress, correspondingly, increases by 10–15% in the presence of the primary structure (closed symbols in figure 20a).

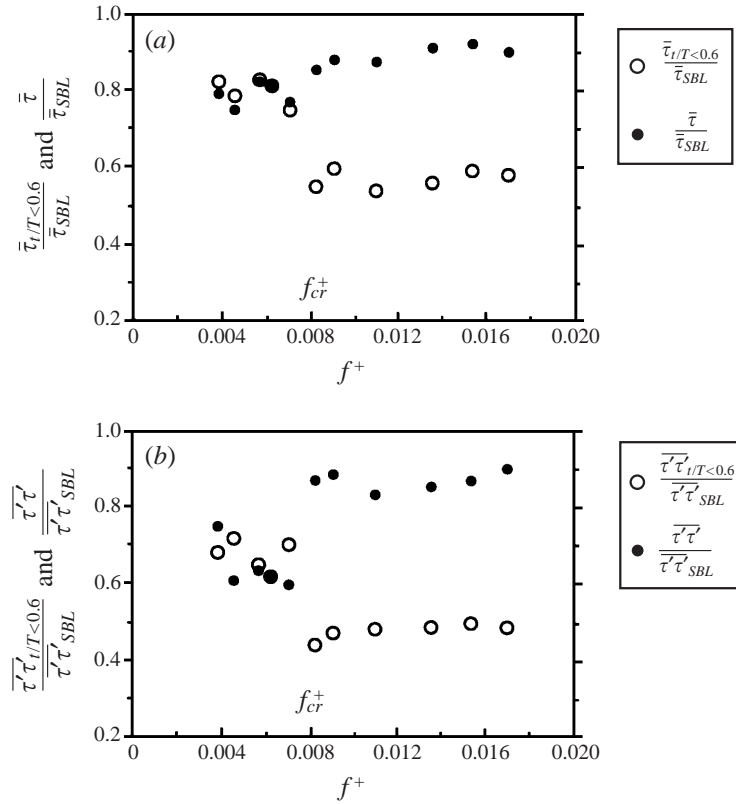


FIGURE 20. (a) The ‘mean’ wall shear stress, and (b) its intensity, at $t/T < 0.6$, prior to the arrival of the primary structure at $x^+ = 120$, versus the imposed frequency. The closed symbols correspond to conventional averages.

The wall shear stress intensity $\overline{\tau'\tau'}_{t/T < 0.6}$ distribution shown in figure 20(b) leads to a similar conclusion. Figure 20(b) shows once more the singular modification of the near-wall turbulence activity near the critical frequency.

The variations of the time-mean skewness $S_{du'/dt}$ at $y^+ = 12$ as a function of f^+ are reported in figure 21. It is seen that the skewness decreases drastically once $f^+ > f_{cr}^+$ and reaches the local ‘isotropic’ value as discussed in § 3.1. Significantly, low $\langle S_{du'/dt} \rangle$ was observed at the end of the acceleration phase for all the experiments performed at f^+ larger than the critical frequency. For low frequencies, correspondingly $\langle S_{du'/dt} \rangle$ was hardly modulated, and the time-mean skewness was very close to the SBL value. There is some trend for $S_{du'/dt}$ to decrease at $f^+ < f_{cr}^+$ in figure 21. Yet, the sudden decrease near the critical frequency is noteworthy. The alteration of the buffer layer nonlinearity is therefore related to high-frequency oscillating blowing. Some further comments on these effects are provided in § 4.4.

The flow mechanism at high imposed blowing frequencies is summarized in figure 22. The blowing induces a positive wall vorticity layer that hardly diffuses beyond the low buffer layer. Its first effect is to counterattack the existing negative vorticity and consequently to relaminarize the flow. Once $\omega'_{zCOH} > 0$ is strong enough, it rolls up into a coherent spanwise vortex. Then a penalty results, because Ω'_{zCOH} induces a negative vorticity layer near the wall. The latter increases the shear, and at the same time, triggers the wall turbulence activity. Further downstream, the negative vorticity

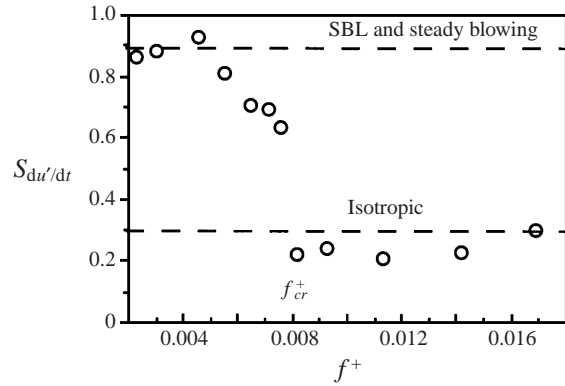


FIGURE 21. Time-mean skewness of du'/dt at $y^+ = 12$ versus the imposed frequency.

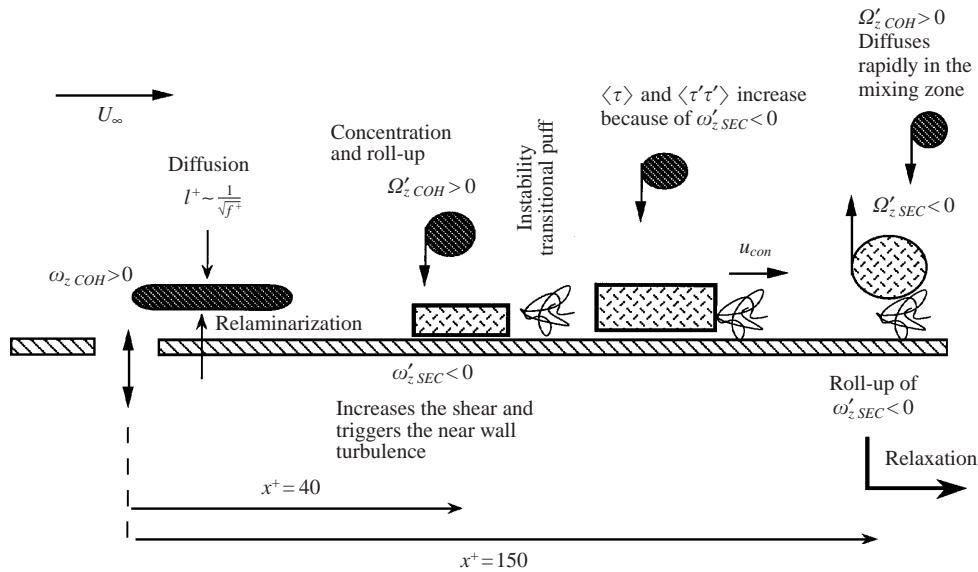


FIGURE 22. Mechanism at high imposed blowing frequencies.

layer rolls up in its turn. The secondary structure, whose effect is the opposite of the primary one, accelerates the relaxation. Some physical insights into this phenomenon will be discussed in § 4.3.

3.7. Efficiency of localized unsteady blowing as a probing strategy

The efficiency of localized unsteady blowing as a probing method discussed in § 1 will now be discussed. Recall that the aim of the probing is to reduce the uncertainties, enhance future decisions and decrease the amount of cautious control. Its efficiency is related to the post-update state covariance matrix of the system parameters, i.e. the covariance estimate after probing had been applied at a given step. The determination of this matrix is not possible here, since we only analyse an open-loop system. However, we can intuitively claim that the prediction will be related to $\langle \tau' \tau' \rangle$ in a closed-type algorithm including the unsteady local blowing as probing control. Low phase averages of wall shear stress intensities resulting from the 'probing' will obviously improve the future state estimates and control actions. The error of a

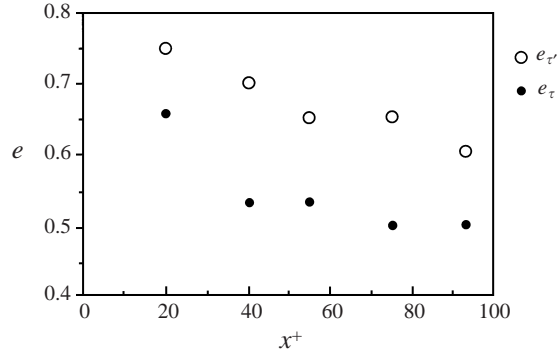


FIGURE 23. Efficiency of high-frequency localized blowing on the wall shear and its turbulent intensity versus the streamwise distance from the slot. This quantity is the percentage of time the intensity and shear remain below the quasi-steady values.

one-step predictor is related to the τ' spectra $S_{\tau'}(\omega)$ by:

$$E = \exp \left\{ \frac{1}{f_k} \int_0^{f_k} \ln S_{\tau'}(\omega) d\omega \right\},$$

according to the Kolmogorov formula where f_k stands for the Kolmogorov frequency. That shows how the reduction of $\langle \tau' \tau' \rangle$ enhances the prediction. According to figure 12(b), $\langle \tau' \tau' \rangle / \overline{\tau' \tau'}_{SBL} < 1$ until $x^+ = 75$. This criterion alone is not sufficient to decide on the efficiency of high-frequency unsteady blowing. The same reduction could be, for instance, obtained by low-frequency, quasi-steady blowing too. For that reason, we defined another efficiency criterion. Thus, we computed the amount of time that $\langle \tau' \tau' \rangle$ is smaller than the wall shear stress intensity that would result from quasi-steady blowing (QS) at the corresponding injection velocity $\langle v_0 \rangle$ and streamwise distance. Denoting this by $\langle \tau' \tau' \rangle_{QS}$, we define the efficiency $e_{\tau'}$ by:

$$e_{\tau'} = \sum N_i / N \quad \text{with } N_i = 1 \text{ if } \langle \tau' \tau' \rangle < \langle \tau' \tau' \rangle_{QS},$$

and $N_i = 0$ otherwise,

where N is the total number of channels (discrete time periods) defining the phase average. Clearly $e_{\tau'}$ is the percentage of time $\langle \tau' \tau' \rangle < \langle \tau' \tau' \rangle_{QS}$, during the oscillation cycle. Figure 23 shows the results obtained in the high-frequency regime $f^+ > f_{cr}^+$. It is seen that the wall shear stress intensity phase averages are smaller than $\langle \tau' \tau' \rangle_{QS}$ during 70% of the time for $x^+ < 75$. The ratio $\langle \tau' \tau' \rangle / \langle \tau' \tau' \rangle_{QS}$ is smaller than 0.5 for some 50% of these time periods. In terms of system parameter estimations, the efficiency for the wall shear stress intensity is more important than the efficiency for drag in a probing strategy. The quantity e_{τ} defines the efficiency for the wall shear stress, in a similar manner and is also shown in figure 23. The drag efficiency is about 0.5.

Thus, the probing by high-frequency localized blowing can be quite efficient in the zone $x^+ < 75$. The spacing between MEMS used in the cautious part of an envisaged dual control scheme (figure 1) can be increased by an order of magnitude. As pointed out in the previous sections, this efficiency results from the confinement of the positive ω'_{zCOH} vorticity layer to near the wall, which counterattacks the existing vorticity distribution and stabilizes the turbulence activity. The penalty is the roll-up resulting in large $\langle \tau' \tau' \rangle / \overline{\tau' \tau'}_{SBL}$ at $x^+ > 75$ and for some t/T . Therefore, another

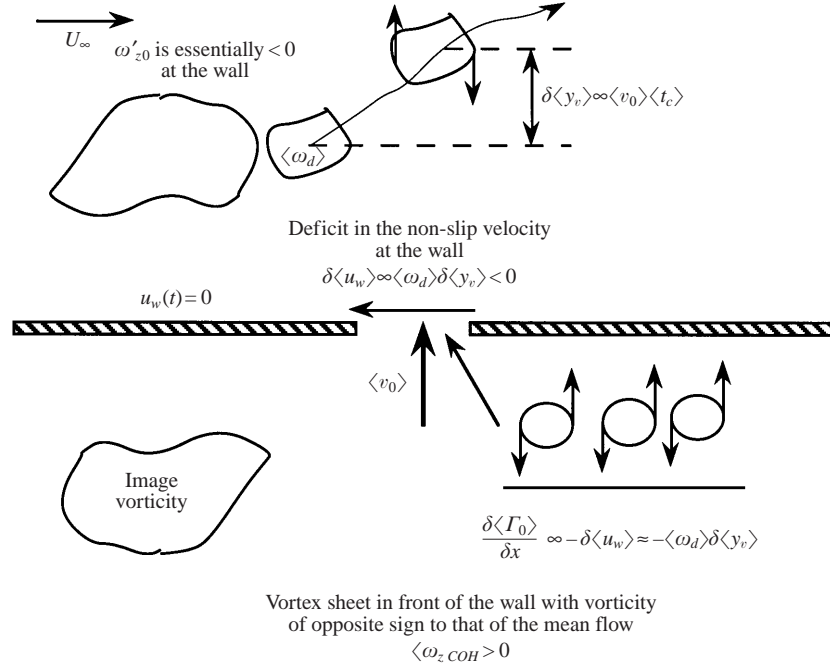


FIGURE 24. Schematic representation of the physical effect of unsteady blowing. The distribution of vorticity in the flow is such that the induced velocity at the wall $u_w(t) = 0$ instantaneously. The blowing causes a deficit of the non-slip velocity corrected by a vortex sheet. The associated vorticity $\omega_{zCOH} > 0$ rolls up into Ω_{zCOH} in the high-frequency regime and during the deceleration phase.

probing strategy has to be adopted at this station to delay the effect of the primary structure. One way to prevent the roll-up of the retrograde spanwise vortex Ω'_{zCOH} may be the use of time-periodical phase-shifted blowing–suction somewhere near $x^+ = 75$. Another possibility is to investigate the effect of nonlinear time-periodical localized blowing, by fast step acceleration (to relaminarize) followed by smooth deceleration (to stabilize). Both possibilities will be analysed in the future. This gives some future perspectives. The only way of determining the whole probing strategy is by experimentation.

4. Discussion

4.1. Main physical mechanism of local unsteady suction–blowing

The management of near-wall turbulence by unsteady suction/blowing is closely related to the flux of vorticity induced locally at the wall. Consider the phase-averaged streamwise equation of momentum over the slit:

$$\langle v_0 \rangle \frac{\partial_0 \langle u \rangle}{\partial y} = -\frac{1}{\rho} \frac{\partial \langle p_0 \rangle}{\partial x} + v \frac{\partial_0^2 \langle u \rangle}{\partial y^2} - \frac{\partial \langle u'v' \rangle_0}{\partial y} = -\frac{1}{\rho} \frac{\partial \langle p_0 \rangle}{\partial x} + v \frac{\partial_0^2 \langle u \rangle}{\partial y^2},$$

since $\langle u'v' \rangle \propto y^2$ near the wall. In this expression, u and v denote the streamwise and wall normal velocity components in the x - and y -directions, respectively, p is the pressure and primes indicate fluctuating quantities as usual. The zero subscript refers to quantities computed at the wall. Noting that the phase-averaged spanwise vorticity at the wall is $\langle \omega_{z0} \rangle = (\partial_0 \langle v \rangle / \partial x) - (\partial_0 \langle u \rangle / \partial y) \approx -\partial_0 \langle u \rangle / \partial y$, because $\partial_0 \langle v \rangle / \partial x$ can be

neglected except near the ends of the slit, we have:

$$\langle v_0 \rangle \langle \omega_{z0} \rangle = \frac{1}{\rho} \frac{\partial \langle p_0 \rangle}{\partial x} + v \frac{\partial_0 \langle \omega_z \rangle}{\partial y},$$

which expresses the simple fact that there is equilibrium between the advection of vorticity through the slit and flux of vorticity at $y = 0$. In the case of suction, there is a real physical removal of spanwise vorticity from the wall and the flux of vorticity is positive, since $\langle v_0 \rangle < 0$ and $\langle \omega_{z0} \rangle < 0$ as in a boundary layer with favourable pressure gradient. The vorticity withdrawn by suction is rapidly replaced at the wall to keep the non-slip condition in force, so that there is a rapid generation of vorticity, say $\delta \langle \omega_{z0} \rangle$ of the same sign as in the incoming flow. Consequently, the flow accelerates by an amount that is approximately $\delta \langle u \rangle / \delta x \propto -(\delta \langle \omega_{z0} \rangle / \delta x) y > 0$, resulting in a local increase of the wall shear stress. Although it is well known that suction is qualitatively similar to flows with favourable pressure gradients, the former is fundamentally different in turbulent boundary layers because it additionally involves the removal of both streamwise and wall normal vorticity.

In blowing, there is no removal or addition of vorticity, but we may still argue that there is a flux of vorticity that is now negative as in the adverse pressure gradient case. The mean and instantaneous spanwise vorticity (which is skewed to negative values near the wall), together with vortical intensive energetic structures are displaced and pushed away from the wall by say $\delta \langle y_v \rangle \propto \int_t^{t+(t_c)} \langle v_0 \rangle dt$, where $\langle t_c \rangle$ is the effective convection time of the structures over the slit. The convection time may be estimated as $t_c^+ \sim L_x^+ / u_c^+$ with u_c^+ and L_x^+ being, respectively, the typical convection velocity and the streamwise extent of the slit in wall units. We have shown in § 3.2, that the effect of the imposed unsteadiness is confined to the low buffer layer. It is therefore logical to consider that the convection velocity is typically the local velocity at $y^+ \sim 10$, which gives $t_c^+ \sim 1$ under the present experimental conditions. This value is significantly smaller than the blowing oscillation period $T^+ = 59$. Consequently, the vorticity displacement may be written here as $\delta \langle y_v \rangle \propto \langle v_0 \rangle \langle t_c \rangle$. Denoting by $\langle \omega_d \rangle$ the amount of vorticity pushed away from the wall, it is easy to realize that the net effect is an induced deficit of $\delta \langle u_w \rangle \propto \langle \omega_d \rangle \delta \langle y_v \rangle < 0$ in the non-slip velocity at the wall. The latter is subsequently corrected by the formation of a thin vortex sheet in front of the wall and of its image with vorticity of opposite sign to that existing in the flow (see figure 24). The strength of this sheet may be estimated as $\delta \langle \Gamma_0 \rangle / \delta x \propto -\delta \langle u_w \rangle \approx -\langle \omega_d \rangle \delta \langle y_v \rangle$. The vorticity sheet is subsequently diluted through diffusion. Thus, the wall shear stress decreases and the flow decelerates near the wall. This phenomenon takes place over and just upstream of the local blowing station. The zone downstream of the slit is concerned with the relaxation of the turbulence structure modified by the discontinuous intervention. Note that the arguments presented here are based solely on the spanwise vorticity and exclude the effect on the quasi-streamwise energy-producing eddies. The analysis is, therefore, not complete, but it may provide a first schematic model to give insight to a complex phenomenon.

4.2. Equivalence between steady and unsteady blowing

We will now discuss the equivalence between the unsteady and steady blowing with the same time mean blowing severity parameter in terms of boundary conditions, i.e. vorticity flux. First, note that the pressure gradient term $\partial \langle p_0 \rangle / \partial x$ is retained in the streamwise momentum equation given above. In Falkner–Skan type flows, the boundary-layer approximation is often used, and a specific distribution of suction–blowing velocity is required to obtain similarity solutions. In other sam-

ple computations dealing with steady discontinuous viscous suction, the pressure gradient is ignored at first glance (Sherman 1990, p. 372). These important terms require full computation, but it is logical to neglect them in an approximate qualitative analysis. Furthermore, there is an additional complexity in the case of unsteady blowing, because the wall normal velocity induces an oscillating pressure gradient without any flux of vorticity according to the wall normal momentum equation over the slit, i.e. $\partial\langle v_0 \rangle / \partial t = -(1/\rho)(\partial\langle p_0 \rangle / \partial y)$. This may throw doubt on the boundary-layer approximation near the slit. However, the main mechanism is still the flux of vorticity under the present working conditions. With a sinusoidal blowing velocity $\langle v \rangle_0^+ = \hat{A}^+(1 - \cos \omega^+ t^+)$ expressed in wall units, we have $\partial\langle p_0^+ \rangle / \partial y^+ \sim \hat{A}^+ \omega^+$ while the flux of vorticity is $\partial_0\langle \omega_z^+ \rangle / \partial y^+ \sim \hat{A}^+$. The maximum imposed frequency in this study is $\omega^+ = 0.1$, which shows that the wall normal oscillating pressure gradient is an order of magnitude smaller.

According to these remarks, the time-mean streamwise momentum equation reduces to:

$$\bar{v}_0 \bar{\omega}_{z0} + [\overline{\tilde{v}_0 \tilde{\omega}_{z0}}] = \frac{1}{\rho} \frac{\partial \bar{p}_0}{\partial x} + \nu \frac{\partial_0 \bar{\omega}_{z0}}{\partial y} \approx \nu \frac{\partial_0 \bar{\omega}_{z0}}{\partial y},$$

when the blowing is unsteady. The time-mean severity parameter is fixed the same in this study for steady and periodical blowing runs. That does not ensure the same flux of vorticity, however, mainly because of the ‘streaming’ quantity $\overline{\tilde{v}_0 \tilde{\omega}_{z0}}$ in the brackets of the preceding equation but also because the mean streamwise vorticity can be different under steady and unsteady blowing conditions at the injection slot. It turns out that, in the high-frequency regime $f^+ = 0.017$ detailed in this paper, the time-mean wall shear stress is not affected near the slit (until $x^+ = 40$ downstream) and that the modulation $\tilde{\omega}_{z0}$ is approximately in quadrature with the injection velocity \tilde{v}_0 . This behaviour may be explained by the fact that the diffusing vorticity is in quadrature with the flux of vorticity in the high-frequency regime to the first order as in Stokes flow over an oscillating flat plate. This may be rigorously shown through a method given by Schlichting (1979 p. 428) but the details will be omitted here. Therefore, $\overline{\tilde{v}_0 \tilde{\omega}_{z0}}$ is 6 times smaller than $\bar{v}_0 \bar{\omega}_{z0}$ and the ‘streaming’ appearing in the boundary conditions may be neglected. In the high-frequency case, therefore, there is equivalence between time-mean injection velocities and time-mean vorticity fluxes.

4.3. Roll-up mechanism

The roll-up of the sheet of vorticity, set-up at the wall to counterattack the effect of blowing, is strongly frequency dependent. This process is not due to an unsteady separation phenomenon, and takes place at high-imposed frequencies, as we have shown in §3.6. The birth of $\Omega_{zCOH}^+ > 0$ discussed in §3.3 is due to the accumulation of vorticity during the oscillation period. The intensification is, indeed, one of the necessary conditions of the roll-up (Jiménez & Orlandi 1993).

It has been argued in §4.1 that local blowing, pushing the mean vorticity and coherent Reynolds shear stress producing eddies away from the wall, creates a deficit in the non-slip velocity. The latter has been connected to the displacement of the structures that has been estimated as $\langle \delta y_v \rangle \sim \langle v_0 \rangle \langle t_c \rangle$, provided that the effective convection time $\langle t_c \rangle$ is significantly smaller than the imposed period T , as is the case here. Therefore, the time-mean displacement in wall units is $\overline{\delta y_v^+} \sim \bar{v}_0^+ \bar{t}_c^+ + \overline{\tilde{v}_0^+ \tilde{t}_c^+}$. In a similar way, the circulation of the fresh vortex sheet generated at the wall to reinforce the no-slip condition is $\bar{\Gamma} \sim L_x \bar{\omega}_d \overline{\delta y_v} + L_x \overline{\tilde{\omega}_d \tilde{\delta y_v}}$, at the mean. It is recalled that ω_d stands symbolically for the vorticity displaced by blowing, and that L_x is

the slot width. That the wall shear stress decreases in the immediate vicinity of the slot is clearly due to the back diffusing vorticity layer, i.e. $\overline{\Delta\tau}^+ \sim \bar{\Gamma}^+$. Combining and neglecting the streaming terms such as $\overline{\tilde{v}_0^+ \tilde{t}_c^+}$, at first glance, we obtain a simple estimation, namely $\overline{\Delta\tau}^+ \sim L_x^+ \bar{\omega}_d^+ \bar{v}_0^+ \bar{t}_c^+$, which should be valid as long as the structure of the flow is not profoundly altered, i.e. when there is no separation or roll-up. Recall that the diffusing vorticity layer has been denoted by ω'_{zCOH} in §3.3.

We have shown in §3.6 (figure 17) that the phase averages of $\langle \tau \rangle$ and the mean decrease in the shear are reasonably independent of the imposed frequency at $x^+ < 40$, as long as f^+ remains below a critical value at which the roll-up takes place. According to the arguments given in the previous paragraph, the strength $\bar{\Gamma}^+$ of the vorticity layer generated in front of the slot is also insensitive to f^+ before the set-up of the roll-up.

The generated vorticity diffuses back out into the fluid to a distance $l^+ \sim \sqrt{t^+}$ in time t^+ . The timescale is imposed by the oscillations, i.e. $t^+ \sim 1/f^+$, therefore, $l^+ \sim 1/\sqrt{f^+}$. Thus, the thickness of the region into which $\bar{\Gamma}^+$ diffuses decreases with imposed frequency. Recalling that $\bar{\Gamma}^+$ is insensitive to f^+ , we deduce that the same amount of vorticity is diluted into a zone increasingly confined, as the frequency becomes large. Thus, it accumulates during the oscillation period, concentrates, and becomes confined in a thin layer near the wall. Its first effect is the time-local relaminarization in the immediate vicinity of the slot. Slightly further downstream, the discontinuity in the vorticity distribution causes it to roll up into Ω'_{zCOH} .

In a turbulent boundary layer, the vorticity is diffused by viscosity away from the wall until reaching roughly $y^+ = 7$, at which point turbulence diffusion is important. We have shown in figure 18 and §3.6 that the critical frequency beyond which the coherent spanwise structure $\Omega'_{zCOH} > 0$ appears is $f_{cr}^{+*} = 14 \times 10^{-3}$ when scaled with the local shear velocity. This corresponds to a diffusion distance of $l^{+*} = 8.5$ in local variables. Thus, viscous diffusion alone governs the removal of the unsteady vorticity layer from the wall in this regime and the turbulence does not participate in the diffusion.

4.4. Further discussion on the effect on the fine structure

We now return to the peculiar behaviour of the phase-averaged skewness shown in figure 8(b) and draw attention again to the negative values of $\langle S_{du'/dt} \rangle$ occurring during the acceleration phase. This behaviour is in total contradiction with the time-mean profiles $S_{du'/dt}$ of the standard boundary layer where $S_{du'/dt}$ reaches large positive values near the wall. The skewness factor of du'/dt appears in the equation for the mean-square vorticity of the isotropic homogeneous turbulence, i.e.

$$\frac{d\overline{\omega'^2}}{dt} = \frac{7}{3\sqrt{5}} S_{du'/dt} \overline{\omega'^2}^{3/2} - 10\nu \left(\frac{\partial \overline{\omega'}}{\partial x} \right)^2$$

(Batchelor 1953). The vorticity production term is proportional to $S_{du'/dt}$. Positive values of this term mean production by stretching, whereas negative values indicate destruction by compression that rapidly suppress any turbulence activity that cannot be maintained. The results presented in figure 8(b) suggest that suppression of streamwise vorticity is plausible in the manipulated boundary layer. This conjuncture is subject to the nature of the near-wall turbulence being highly anisotropic and inhomogeneous. The observed effects are, however, so severe that a strong alternation of the vorticity generation mechanism is certain.

Although $\langle S_{du'/dt} \rangle < 0$ shows strong interactions of the imposed unsteadiness with

the nonlinearity near the wall, the streamwise stretching is undoubtedly not the only activity in the generation of the streamwise vorticity. Moreover, its effect is negligible regarding the tilting of wall normal vorticity ω'_y near the wall (Brooke & Hanratty 1993; Jiménez 1994). The effect of unsteady blowing may be better captured, at least qualitatively, by examination of the instantaneous equation governing ω'_y :

$$\frac{D\omega'_y}{Dt} = \omega'_x \left[\frac{\partial \langle v \rangle}{\partial x} + \frac{\partial v'}{\partial x} \right] + \omega'_y \left[-\frac{\partial \langle u \rangle}{\partial x} + \frac{\partial v'}{\partial y} \right] + \left[\omega'_z - \frac{\partial \langle u \rangle}{\partial y} \right] \frac{\partial v'}{\partial z} + \nu \nabla^2 \omega'_y,$$

where we made use of the continuity $\partial \langle v \rangle / \partial y = -\partial \langle u \rangle / \partial x$. The stretching term of ω'_y is $\omega'_y [-(\partial \langle u \rangle / \partial x) + (\partial v' / \partial y)]$. Since the effect of blowing near the wall and over the slit is a local deceleration $\partial \langle u \rangle / \partial x < 0$, it is seen that positive ω'_y is enhanced by wall normal stretching $\partial \langle v \rangle / \partial y > 0$ while negative ω'_y is compressed and rapidly disappears by viscous diffusion. The somewhat enhanced $\omega'_y > 0$ is tilted to positive streamwise vorticity $\omega'_x > 0$ by the shear according to:

$$\frac{D\omega'_x}{Dt} = \omega'_x \left[\frac{\partial \langle u \rangle}{\partial x} + \frac{\partial u'}{\partial x} \right] + \omega'_y \left[-\frac{\partial \langle u \rangle}{\partial y} + \frac{\partial u'}{\partial y} \right] + \left[\omega'_z - \frac{\partial \langle u \rangle}{\partial y} \right] \frac{\partial u'}{\partial z} + \nu \nabla^2 \omega'_x$$

through the second term of this equation, but is then compressed by $\partial \langle u \rangle / \partial x < 0$ and is subsequently weakened in its turn. The consequent destruction of ω'_x which leads to that of the coherent quasi-streamwise vortices is connected with the decorrelation of u' and v' and results inevitably in relaminarization. This fractional scenario, in which first the wall normal vorticity is stretched and tilted to streamwise vorticity that is stretched in its turn, is in perfect agreement with the model suggested by Jiménez (1994). In an accelerating flow, the situation is inverse but the conclusion is the same. It is well known that both accelerating and decelerating flows may lead to relaminarization, if the necessary precautions are taken to prevent the flow separation in the latter case (Narasimha & Sreenivasan 1979).

5. Conclusion

The effects of an oscillating localized blowing on near-wall turbulence is investigated. The imposed frequency is twice as large as the ejection frequency of the inner layer, and the blowing amplitude is 5 wall units. The severity parameter is low, excluding any phenomena related to unsteady flow separation.

The ingredients characteristic of relaminarization are present near the slot at $x^+ < 40$ and during half of the cycle, namely:

- (i) The wall shear stress decreases considerably until reaching the value that a laminar boundary layer would have at the same Reynolds number.
- (ii) Dissipation dominates the near-wall flow which is stabilized.
- (iii) The velocity fluctuations in the inner layer are not zero, but their contribution to the dynamics of the flow becomes inconsequential.
- (iv) The frequency of active Reynolds-stress-producing events decreases considerably and a thin region near the wall extending to approximately 2–3 wall units grows from the wall, being free of fluctuating streamwise vorticity. The thickness of this zone reaches almost 5 wall units during half of the oscillation cycle.
- (v) The stretching of quasi-streamwise vorticity decreases strongly, as indicated by negative values of the skewness of the streamwise velocity fluctuation time derivatives. This part of the oscillation cycle also coincides with large decreases of the Taylor timescale, indicating the appearance of small-scale turbulence.

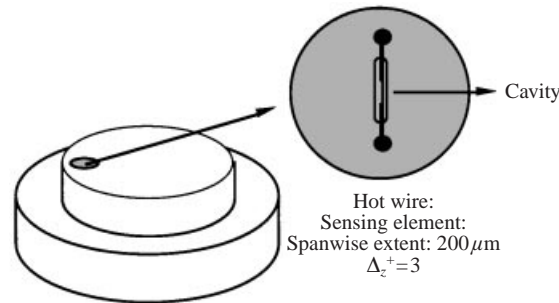


FIGURE 25. Sketch of the Cousteix–Houdeville probe used in this investigation.

The main effect of blowing is the displacement of the spanwise vorticity and the turbulent-drag-inducing quasi-streamwise vortical structures (QS) away from the wall. This phenomenon is associated with the formation of a thin vortex sheet in front of the wall (and of its image) with vorticity of opposite sign to the mean vorticity. This sheet subsequently dilutes through diffusion. It turns out that, in the deceleration phase and when the imposed unsteadiness is sufficiently rapid, there is a net accumulation of this sheet, leading to a coherent spanwise structure after roll-up. This phase coincides with the uncoupling of the near-wall flow and the removed QSVs, resulting in a temporal relaminarization. The near-wall part of this structure has a spanwise vorticity layer of the same sign as the mean flow. Consequently, the wall shear stress increases in a cyclic manner at $x^+ > 75$, at times and locations that are perfectly predictable. This induced secondary vorticity layer rolls over in its turn by an essentially similar mechanism. The secondary spanwise structure has an effect opposite to the primary one. It decreases rapidly the peaks of the wall shear stress and accelerates the relaxation process. These are real unsteady effects occurring only when the blowing frequency is larger than a critical value. The ensemble of the results presented here shows how a time-varying intervention at the wall may involve complex phenomena. It is hoped that they may provide new perspectives on near-wall control, through a combination of phase-shifted and eventually frequency-modulated local blowing/suction sites.

The phenomena reported in this paper are confined mainly to the low buffer and viscous sublayers in the high-frequency regime. Detailed measurements of the entire Reynolds shear stress tensor components in this zone are difficult, and so are flow visualizations under the present experimental conditions. The primordial development of three-dimensional effects involved in setting up the instabilities could therefore not really be detailed. Experimental facilities (such as the Eckelmann's oil channel) wherein a relatively thick sublayer is available could allow the obtaining of information that is more detailed. Direct numerical simulations even in the minimum channel would also be of great help. Time-periodical nonlinear blowing–suction waveforms must also be investigated in order to determine the most efficient probing strategy.

Appendix A. Validation of the wall shear stress measurements

The frequency response of the hot-wire gauge in the micro-cavity (figure 25) is carefully checked by comparing the measured statistics of the fluctuating wall shear stress $\tau'(t)$ in a canonical non-manipulated boundary-layer flow with existing data. The results are summarized in figures 26 and 27. The ratio of the turbulent wall

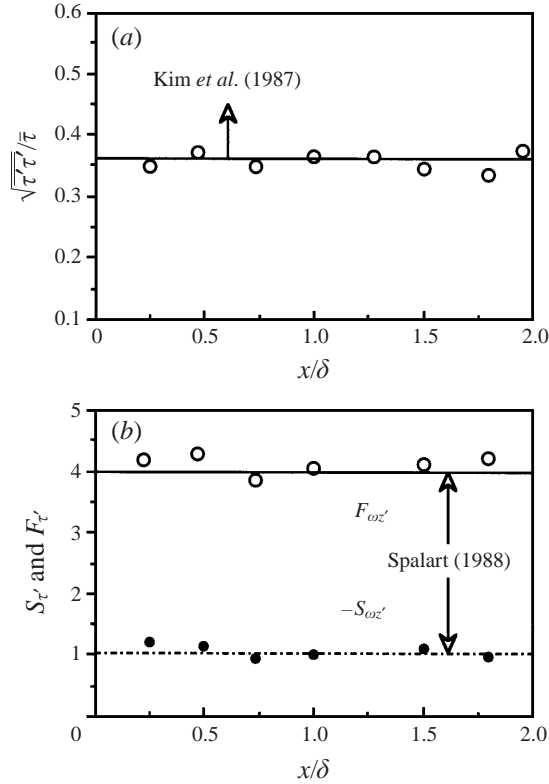


FIGURE 26. (a) Wall shear stress intensity divided by the time mean wall shear stress versus the streamwise distance from the slot. (b) Flatness and skewness of instantaneous wall shear stress compared with the DNS results of Spalart (1988).

shear stress intensity $\sqrt{\overline{\tau'\tau'}}$ to the local wall shear stress $\bar{\tau}$ versus the distance x/δ is shown in figure 26(a). Here, δ denotes the local boundary-layer thickness, as usual, and $x = 0$ corresponds to $X = 1.14$ m from the leading edge. It is seen in figure 26(a) that $\sqrt{\overline{\tau'\tau'}}/\bar{\tau} = 0.35 \pm 0.025$ is in good agreement with Kim *et al.* (1987). Since $\sqrt{\overline{\tau'\tau'}}/\bar{\tau} = \sqrt{u'u'}/\bar{U}$ as $y \rightarrow 0$, the wall shear stress intensity may also be compared with careful measurements very close to the wall. Such measurements have been reported by Durst, Jovanovic & Sender (1993) who give $\sqrt{u'u'}/\bar{U} \approx 0.36$ at $y^+ = 1$. This result alone may be sufficient to certify the satisfactory response of the wall gauge. Recall that values as low as 0.06 (1983), due to the effect of the heat conduction into the substrate, have been reported in the literature.

The high-order statistics, i.e. the skewness $S_{\tau'} = \overline{\tau'^3}/\overline{\tau'}^3$ and the flatness $F_{\tau'} = \overline{\tau'^4}/\overline{\tau'}^4$ of $\tau'(t)$ were also measured. The results are shown in figure 26(b). It was found that, in the standard boundary layer, $S_{\tau'} \approx 1$ and $F_{\tau'} \approx 4$. Measurements of high-order statistics are seldom reported in the literature, and, hence, a comparison is not feasible. As an alternative, we compare with the DNS results of Spalart (1988) and use the simple relationship between the $(S_{\tau'}, F_{\tau'})$ and $(S_{\omega'z'}, F_{\omega'z'})$, where $\omega'_{z,0} = -(\partial u'/\partial y)_{y=0}$ is the fluctuating spanwise vorticity at the wall, since $S_{\tau'} = -S_{\omega'z,0}$ and $F_{\tau'} = F_{\omega'z,0}$. According to Spalart, $S_{\omega'z,0} = -1$ and $F_{\omega'z,0} = 4$. These quantities are, of course, consistent with the asymptotic values of the skewness and flatness of

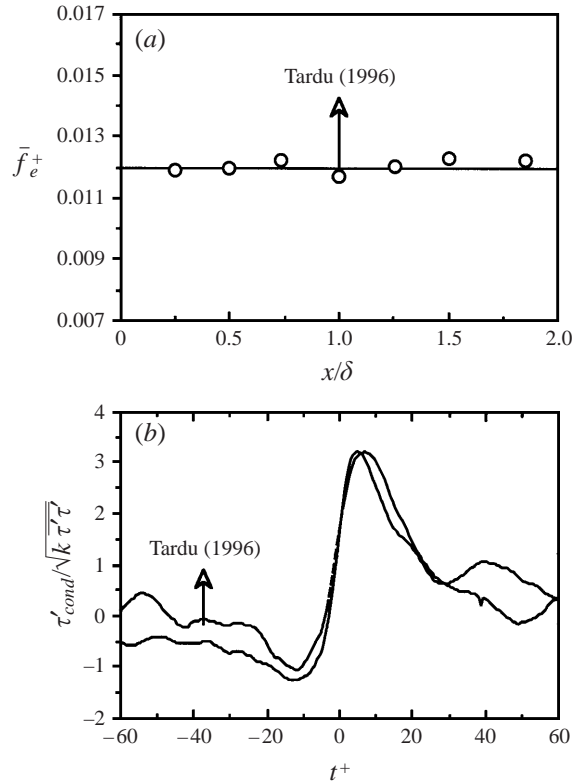


FIGURE 27. (a) The frequency of VITA events detected by the probe.
 (b) The resulting conditional averages.

streamwise velocity fluctuations as $y^+ \rightarrow 0$. The measured values of the third and fourth moments of $\tau'(t)$ are in close agreement with these results. The estimated errors in the measurements of $S_{\tau'}$ and $F_{\tau'}$ are, respectively, 5% and 8%.

The temporal wall shear stress was further analysed by determining the frequency of the shear-layer events detected by VITA defined in §3.2. The distribution of the time-mean frequency in wall units $\bar{f}_e^+ = \bar{f}_e(v/\bar{u}_\tau^2)$ of the VITA events is shown in figure 27(a). It is seen that $\bar{f}_e^+ \approx 0.012$ and this value coincides well with that obtained by Tardu & Binder (1997) in totally different conditions, namely in a fully developed turbulent water channel at a nearly similar $Re_\theta = 835$ and with a TSI 1268W flush-mounted hot-film gauge. Recall that the wall hot-film measurements in water are reliable, and the frequency response of the thermal boundary layer is satisfactory, because the effect of the heat conduction into the substrate is negligible (see for example Tardu *et al.* 1991). Finally, the conditional averages $\tau'_{cond} / \sqrt{k \tau' \tau'}$ shown in figure 27(b) correspond quite well to the measurements quoted before. These results increase the confidence in the measurements reported in this paper.

Appendix B. Spanwise homogeneity

As indicated in §2.1, the spanwise extent of the blowing slot is $L_2^+ = 1212$ in wall units, large enough to suppose that the flow is homogeneous in this direction. To check to what extent this hypothesis is valid, we took measurements of the wall shear

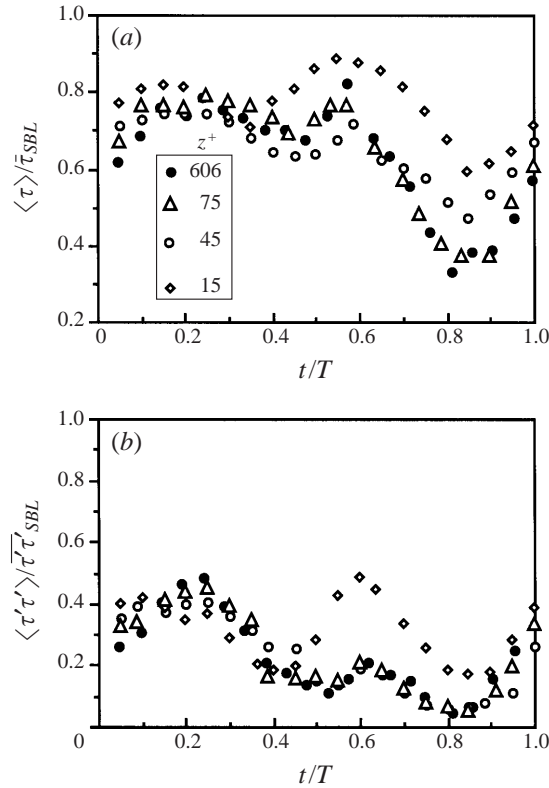


FIGURE 28. Phase averages of (a) the wall shear stress and (b) of its turbulent intensity, at $x^+ = 40$ versus the spanwise distance beginning with the edge of the blowing slot. The imposed frequency is $f^+ = 0.0017$.

stress and the streamwise velocity field at, respectively, $x^+ = 40$ and $x^+ = 120$. They were taken every 15 wall units until $z^+ = 90$ and then every 40 wall units, $z^+ = 0$ corresponding to the edge of the slot. The imposed frequency was $f^+ = 0.0017$. Figures 28(a) and 28(b) show, respectively, the phase averages of the wall shear stress and of its turbulent intensity in the near flow field at $x^+ = 40$. Only a few results are reported here for the sake of clarity. These are independent measurements and the comparison of figure 28 with figure 5 at the middle of the slot $z^+ = 606$ indicates that the results are reproducible. The first observation is the collapse of the phase averages for $z^+ > 75$, indicating that the flow is homogeneous over 86% in span. The effect of the edge discontinuity is clearly perceptible at $z^+ < 45$, especially in the response of $\langle \tau' \tau' \rangle$. This effect rapidly disappears within a distance of $\Delta z^+ = 30$. The peak in $\langle \tau' \tau' \rangle$ at $z^+ = 15$ is quite pronounced. Recall that this peak is attributed to the roll-up of the primary structure, because of the concentration and discontinuity of the vorticity field. It is possible that the edge singularity speeds up this process. The results are similar in the far flow field, the homogeneity being slightly larger, at about 92% in span.

REFERENCES

- ANDERSEN, P. S., KAYS, W. M. & MOFFAT, R. J. 1975 Experimental results for the transpired turbulent boundary layer in an adverse pressure gradient. *J. Fluid Mech.* **69**, 353–375.

- ANTONIA, R. A., KIM, J., BROWNE, L. W. B. 1991 Some characteristics of small-scale turbulence in a turbulent duct flow. *J. Fluid Mech.* **233**, 369–388.
- BAR-SHALOM, Y. 1981 Stochastic dynamic programming: caution and probing. *IEEE Trans. Automatic Control* AC-26, 1184–1195.
- BATCHELOR, G. K. 1953 *The Theory of Homogeneous Turbulence*. Cambridge University Press.
- BEWLEY, T., CHOI, H., TEMAM, R. & MOIN, P. 1993 Optimal feedback control of turbulent channel flow. *Ann. Res. Briefs*, CTR, Stanford University, pp. 3–14.
- BROOKE, J. W. & HANRATTY, T. J. 1993 Origin of turbulence-producing eddies in a channel flow. *Phys. Fluids A* **5**, 1011–1022.
- CHOI, H., MOIN, P. & KIM, J. 1994 Active turbulence control for drag reduction in wall-bounded flows. *J. Fluid Mech.* **262**, 75–110.
- CHOI, H., PARK, J. & HAHN, S. 1997 Effects of blowing/suction from a spanwise slot on a turbulent boundary layer flow. 11th Symp. Turbulent Shear Flows, Grenoble, pp. 1–37.
- DRAZIN, P. G. & REID, W. H. 1981 *Hydrodynamic Stability*. Cambridge University Press.
- DOLIGALSKI, T. L. & WALKER, J. D. A. 1978 Shear layer breakdown due to vortex motion. In *Coherent Structure of Turbulent Boundary Layers* (ed. C. R. Smith & D. E. Abbott), pp. 288–332. Lehigh University, USA.
- DOLIGALSKI, T. L. & WALKER, J. D. A. 1978 The boundary layer induced by a convected two-dimensional vortex. *J. Fluid Mech.* **139**, 1–28.
- DURST, F., JOVONOVIC, J. & SENDER, J. 1993 Detailed measurements of the near wall region of a turbulent pipe flow. In *Turbulent Shear Flows 9* (ed. F. Durst *et al.*), pp. 225–241. Springer.
- ERSOY, S. & WALKER, J. D. A. 1985 Viscous flow induced by counter-rotating vortices. *Phys. Fluids* **28**, 2687–2698.
- GAD-EL-HAK, M. & BLACKWELDER, R. F. 1989 Selective suction for controlling bursting events in a boundary layer. *AIAA J.* **27**, 308–314.
- HILL, D.-C. 1993 Drag reduction at a plane wall. *Ann. Res. Briefs*, pp. 15–19, CTR, Stanford University.
- HILL, D.-C. 1994 Drag reduction strategies. *Ann. Res. Briefs*, pp. 215–218, CTR, Stanford University.
- JIMÉNEZ, J. 1994 On the structure and control of near wall turbulence. *Phys. Fluids* **6**, 944–953.
- JIMÉNEZ, J. & ORLANDI, P. 1993 The roll-up of a vortex layer near a wall. *J. Fluid Mech.* **248**, 297–313.
- KIM, J., MOIN, P. & MOSER, R. 1987 Turbulence statistics in fully developed channel flow at low Reynolds number. *J. Fluid Mech.* **177**, 133–166.
- KLEWICKI, J. C. & FALCO, R. E. 1990 On accurately measuring statistics associated with small-scale structure in turbulent boundary layers using hot-wire probes. *J. Fluid Mech.* **219**, 119–142.
- LEE, C., KIM, J., BABCOCK, D. & GOODMAN, R. 1997 Application of neural networks to turbulence control for drag reduction. *Phys. Fluids* **1**, 1740–1747.
- LIM, J., KANG, S.-M., KIM, J. & SPEYER, J. L. 2000 Application of linear controller to turbulent flows. *20th Intl Congr. Theoret. Appl. Mech. 27 August–2 September 2000, Tech. Rep. Theoretical and Applied Mech. University of Illinois at Urbana-Champaign*.
- LUCHIK, T. S. & TIEDERMAN, W. G. 1987 Timescale and structure of ejections and bursts in turbulent channel flows. *J. Fluid Mech.* **174**, 529–552.
- MAITELLI, A.-L. & YONEYAMA, T. 1999 A multistage suboptimal dual controller using optimal predictors. *IEEE Trans. Automatic Control* **44–45**, 1002.
- NARASIMHA, R. & SREENIVASAN, K. R. 1973 Relaminarization in highly accelerated boundary layers. *J. Fluid Mech.* **61**, 417–447.
- NARASIMHA, R. & SREENIVASAN, K. R. 1979 Relaminarization of fluid flows. *Adv. Appl. Mech.* **19**, 221–309.
- PAILHAS, G., COUSTEIX, J., ANSELMET, F. & FULACHIER, L. 1991 Influence of suction through a slot on a turbulent boundary layer. *Eighth Symp. on Turbulent Shear Flows, Munich*, pp. 18-4-1–18-4-6.
- PAPOULIS, A. 1984 *Probability, Random Variables and Stochastic Processes*, 2nd edn. McGraw-Hill.
- POPOVICH, A. T. & HUMMEL, R. L. 1967 *AICHe J.* **13**, 854–863.
- ROTTA, J. 1950 Das in Wandnähe gültige Geschwindigkeitsgesetz turbulenter Strömungen. *Ing. Arch.* **18**, 277–280.
- SANO, M. & HIRAYAMA, N. 1985 Turbulent boundary layers with injection and suction through a slit. *Bull. JSME*, **28**, 807–814.

- SCHLICHTING, H. 1979 *Boundary Layer Theory*. McGraw-Hill.
- SHEN, S. F. 1961 Some considerations of the laminar stability of incompressible time dependent basic flows. *J. Aero. Sci.* **28**, 397–404.
- SHERMAN, F. C. 1990 *Viscous Flow*. McGraw-Hill.
- SOKOLOV, M. & ANTONIA, R.-A. 1993 Response of a turbulent boundary layer to intensive suction through a porous strip. *Ninth Symp. on Turbulent Shear Flows, Kyoto*, pp. 5-3-1–5-3-6.
- SPALART, P. R. 1988 Direct numerical simulation of a turbulent boundary layer up to $Re_\theta = 1410$. *J. Fluid Mech.* **187**, 61–99.
- STENGEL, R. F. 1994 *Optimal Control and Estimation*. Dover.
- TARDU, S. 1995 Coherent structures and riblets. *Appl. Sci. Res.* **54**, 349–385.
- TARDU, S. & BINDER, G. 1997 Reaction of bursting to an oscillating homogeneous pressure gradient. *Eur. J. Mech. B/Fluids* **16**, 89–120.
- TARDU, S., PHAM, C. T. & BINDER, G. 1991 Effects of longitudinal diffusion and conduction to the substrate on the response of hot film gages—a numerical simulation. In *Advances in Turbulence-3* (ed. A. V. Johansson & P. H. Alfredsson), pp. 506–513. Springer.
- TSE, E. & BAR-SHALOM, Y. 1973 Actively adaptive control for linear systems with random parameters via the dual control approach, *IEEE Trans. Automatic Control*, AC-18, 109–117.
- UEDA H. & HINZE J. O. 1975 Fine-structure turbulence in the wall region of a turbulent boundary layer. *J. Fluid Mech.* **67**, 125–143.
- ZHOU, J., ADRIAN, R. J., BALACHANDAR, S. & KENDALL, T. M. 1999 Mechanisms for generating coherent packets of hairpin vortices in channel flow. *J. Fluid Mech.* **387**, 353–396.